

3D simulations and MLT: II. Onsager’s Ideal Turbulence

W. DAVID ARNETT,¹ RAPHAEL HIRSCHI,^{2,3} SIMON W. CAMPBELL,⁴ MIROSLAV MOCÁK,⁴ CYRIL GEORGY,⁵ CASEY MEAKIN,⁶
ANDREA CRISTINI, LAURA J. A. SCOTT, ETIENNE A. KAISER, AND MAXIME VIALLET

¹*Steward Observatory, University of Arizona, 933 N. Cherry Avenue, Tucson AZ 85721*

²*Astrophysics Group, Keele University, Lennard-Jones Laboratories, Keele, ST5 5BG, UK*

³*Kavli IPMU (WPI), The University of Tokyo, Kashiwa, Chiba 277 8583, Japan*

⁴*School of Physics and Astronomy, Monash University, Clayton, Australia 3800*

⁵*Department of Astronomy, University of Geneva, Ch. Maillettes 51, 1290 Versoix, Switzerland*

⁶*Meakin Technologies, Pasadena, CA 91104*

ABSTRACT

We simulate convective turbulence in stars, extending Arnett, et al (2019). Our implicit large eddy simulations (ILES) use the 3D Euler equations with shock capturing (Colella & Woodward 1984); we simulate an astrophysically-appropriate inviscid limit ($\text{Re} \lesssim 7000$) with causal time stepping but no explicit viscosity. Anomalous dissipation of turbulent kinetic energy occurs as an emergent feature of advection (“Onsager damping”), a physical process caused by the moderate shocks, which terminate the turbulent kinetic energy spectrum. This differs from incompressible turbulence in which nonlinear fluid effects involving vorticity are supposed to control dissipation (Taylor 1937; P. Johnson 2021a). In strongly stratified stellar convection the asymptotic limit for the global damping length of turbulent kinetic energy is $\ell_d \sim \langle u^3 \rangle / \langle \epsilon \rangle$. This “dissipative anomaly” (Onsager 1949) fixes the value of the “mixing length parameter”, $\alpha = \ell_{\text{MLT}} / H_P = \overline{\Gamma_1}$, which is $\sim 5/3$ for complete ionization. The estimate is numerically robust, agrees to within $\sim 10\%$ with estimates from stellar evolution with constant α . For weak stratification ℓ_d shrinks to the depth of a thin convective region. For stellar atmospheres computed with “hyperviscosity stabilization” and variable Γ_1 in regions of partial ionization, the agreement is $\sim 20\%$ (Magic, Weiss, & Asplund 2016). Our ILES are filamentary, produce surfaces of separation at boundary layers, resolve the energy-containing eddies, and develop a turbulent cascade down to the grid scale (which agrees with the 4096^3 direct numerical simulations (DNS) of Kaneda, et al 2003). The cascade converges quickly (Onsager 1949), and satisfies a power-law velocity spectrum similar to (Kolmogorov 1941). Our ILES exhibit intermittency, anisotropy, and interactions between coherent structures, features missing from K41 theory. We derive a dissipation rate from Reynolds stresses which agrees with (i) our ILES, (ii) experiments (Warhaft 2002), and (iii) high Reynolds number DNS of the Navier-Stokes equations (Iyer, et al. 2018; Sreenivasan 2019).

1. INTRODUCTION

We continue our study of stellar convection (Paper I, Arnett, et al 2019). We solve the *three-dimensional (3D), compressible Euler equations* (conservation of mass, momentum, and energy; see §2, Appendix §A; Landau & Lifshitz 1959), with a finite volume scheme

and using the piece-wise parabolic method (PPM) for shock capture (Colella & Woodward 1984). No viscosity is assumed; these astrophysical simulations are inviscid. Minimal assumptions are made concerning flow patterns or boundary layers. These implicit large eddy simulation (ILES) methods were originally developed for supernova and pre-supernova simulations (Fryxell, Müller & Arnett 1989; Bazàn & Arnett 1998), with realistic microphysics for stellar interiors.

Böhm-Vitense (1958) used the “mixing length” theory of Prandtl (Anderson 2005; Biermann 1925), with an adjustable parameter to estimate dissipation, to close the theory of stellar convection; also see §3.3. When ILES

Corresponding author: W. David Arnett

wdarnett@gmail.com, r.hirschi@keele.ac.uk, simwcampbell@gmail.com,
miroslav.mocak@gmail.com, cyril.georgy@unige.ch,
casey.meakin@gmail.com, andrea.cristini89@gmail.com,
l.j.a.scott@keele.ac.uk, e.kaiser@keele.ac.uk, viallet.maxime@gmail.com

(Arnett, Meakin & Young 2009) were applied to this problem a 3D cascade of turbulent energy developed automatically, exhibiting damping in agreement with Kolmogorov (1941), but with *no viscous dissipation defined, and no adjustable parameter needed*. This curious result was due to an “energy-dissipation anomaly” predicted by Onsager (1949), which constrains all convection at high Reynolds number (Re). This is Onsager’s “ideal” turbulence.

The standard approach to turbulence uses the Navier-Stokes (NS) equations, which were designed for laboratory-scale fluid flow (Batchelor 1960; Landau & Lifshitz 1959 §15). Like the Euler equations they enforce conservation of mass, momentum, and energy, but with two added assumptions: incompressibility and molecular dissipation. Both can fail for stars, where large sizes and density stratification occur.

Turbulent flows are classified by a dimensionless ratio, the Reynolds number, $\text{Re} = \ell \Delta u / \nu_{\text{NS}}$, which is the ratio of the inertial term to the dissipation term in the NS equation. Turbulence increases with Re. The characteristic length ℓ (the “integral scale”, or the size of the largest eddies) and the characteristic turbulent velocity Δu are macroscopic properties, while the Navier-Stokes (NS) viscosity ν_{NS} is a measure of molecular dissipation (Pope 2000), a microscopic quantity. At large scale, nonlinear coherent processes can dominate local, collisional ones. As the inviscid limit is approached ($\nu_{\text{NS}} \rightarrow 0$), the NS equations become singular (as $1/\nu_{\text{NS}}$, requiring steep velocity gradients), but not the Euler equations. For solar conditions, we have $\text{Re} \gtrsim 10^{14}$ (Hanasoge, Gizon & Sreenivasan 2016), which implies a tiny effective viscosity. A typical laboratory Re *would be far too small (too viscous) to be realistic for stars*, which are almost “inviscid”.

We find that *dissipation occurs as an emergent feature of nonlinear fluid dynamics (a “dissipative anomaly”)*, as we approach stellar conditions. As this limit is approached (§2.1.2; Eyink & Drivas 2018a), turbulent dissipation is dominated by mild shocks related to the turbulence (Hoffman & Johnson 2008; P. Johnson 2021a).

Our ILES develop a cascade in turbulent kinetic energy which is an extension of the incompressible case (Taylor 1937; Batchelor 1960). Experiments (Warhaft 2002) and direct numerical simulation (DNS, Sreenivasan 2019; Iyer, et al. 2018) have shown that anomalous features are essential to real turbulence: intermittency, coherent structures, and a fluctuating turbulent cascade. We find that these develop automatically in our ILES through the nonlinear advection term. Similar conclusions apply in principle to the NS equations (De Lellis & Sze’kelyhidi 2013; Buckmaster & Vicol

2019; see also Eyink & Drivas 2018a, their Appendix A.2.c, who use a completely different approach involving renormalization-group invariance).

In §2 we examine the theoretical approaches used in (i) our ILES of the Euler equations, and (ii) large eddy simulations (LES) and (iii) DNS of the NS equations. We estimate the effective Reynolds numbers (Re) we attain, and compare specific turbulent kinetic energy (TKE) spectra from simulations.

In §3 we extract from our ILES the flux of turbulent kinetic energy (TKE) in our turbulent cascade, the “dissipative anomaly”. We derive an *analytic* rate of dissipation from a Reynolds stress, which agrees quantitatively with the simulations, and with the conventional dissipation in a turbulent cascade (Kolmogorov 1941). This “dissipative anomaly” is a dynamic constraint on convective flow, requiring a fixed value for the average damping length. For a given driving, turbulence decays (grows) until balanced on average. We examine intermittency due to this approximate balance in TKE around a quasi-steady state.

In §4 we summarize resolution studies (Cristini, et al. 2017; Arnett, et al. 2015) for the case of weakly stratified convection for shell burning of O and of C, both cooled by neutrino pair emission. The simulations develop a dissipation length which agrees with the Reynolds stress value derived in §3, in Arnett, Meakin & Young (2009), and is insensitive to resolution error.

In §5 we examine strong stratification, and find significant acceleration by pressure dilatation (see also Eyink & Drivas 2018a). Sufficiently large stratification leads to a significant negative flux of TKE, unlike MLT. We derive an asymptotic value for the TKE dissipation length in strong stratification at high Re, independent of the dissipation mechanism.

In §6 we discuss astronomical calibration of MLT, from consistency of stellar evolution with the color-magnitude diagram, and conclude that *the apparent “universality” of the mixing-length (Renzini 1987) is a consequence of anomalous dissipation in deeply stratified convection, and our predicted value of $\alpha_{\text{MLT}} = \ell_{\text{MLT}}/H_P = \overline{\Gamma_1} \approx 5/3$ fits the data surprisingly well*. Incomplete ionization and dissociation cause deviations in surface structure and $\overline{\Gamma_1}$; these effects are estimated to be $\pm 20\%$ from simulations stabilized by hyperviscosity (Magic, Weiss, & Asplund 2016).

In §7 we summarize the implications from this and the previous paper (Arnett, et al 2019).

2. METHODS

Among fluid dynamic algorithms for turbulent flow, a key difference lies in the treatment of dissipation.

2.1. Euler equations and ILES

Our library¹ of simulations, previously interpreted within the context of Kolmogorov (1941), have a better interpretation, which we have found in response to reviews regarding “anomalous behavior” (Warhaft 2002; Sreenivasan 2019). We consider the surprising independence of TKE dissipation on viscosity (Onsager 1949; Eyink & Sreenivasan 2006). If the viscous coefficient ν_{NS} is set to zero, reducing the NS equations to the Euler equations, dissipation still occurs, but for physical reasons associated with the nonlinear advection term, not numerical error (§3.4). The reason is related to what mathematicians call the “Onsager conjecture” (De Lellis & Sze’kelyhidi 2013; Buckmaster & Vicol 2019; Isett 2019).

2.1.1. New results: Onsager’s conjecture

In his note on statistical hydrodynamics, Onsager (1949) considered weak solutions² of velocity u in the fluid equations, satisfying the Hölder condition $|u(x, t) - u(x', t)| \leq C|x - x'|^\theta$, where the constant C is independent of x, x' . He conjectured that: (a) any weak solution u satisfying this with $\theta > \frac{1}{3}$ conserves the turbulent kinetic energy, and (b) for any $\theta \leq \frac{1}{3}$ satisfying this, there exist weak solutions u which do not conserve this energy.

This implies a definite rate for dissipation of turbulent kinetic energy in a region with a “rough” (i.e., turbulent) velocity field. This “anomalous dissipation” is independent of viscosity, being a property of turbulence not microphysics (an “Onsager dissipation”).

Further work supports this conjecture (e.g., Constantin & Titi 1994; Duchon & Robert 2000; De Lellis & Sze’kelyhidi 2013; Eyink 2018; Eyink & Drivas 2018a,b; Buckmaster & Vicol 2019; Isett 2019), as do our ILES (Fig. 3, in Arnett, et al. 2015). The precise mechanism of the turbulent energy cascade is becoming clearer. The Taylor (1937) suggestion of “vortex-stretching” (also favored by Onsager 1949), is partially correct, but incomplete. P. Johnson (2021a) finds that “strain-rate self-amplification” (the steepening of compressive strain-rates via nonlinear self-advection, i.e., shocks) also contributes and may dominate the inter-scale transfer of energy in turbulence.

Onsager’s prediction of the non-conservation of turbulent kinetic energy (TKE) is striking: in our ILES,

turbulent dissipation occurs by mild shocks³, which convert TKE into internal energy (§3). *For a given driving, the flow depends upon dissipation which in turn depends implicitly on the flow itself.* This is a statistical constraint with negative feedback and time delay, reflecting both the nonlocality of the process and its connection to intermittency (see e.g., §3.3, Eq. 7). We find that no explicit term need be added to the Euler equations; this damping is provided directly by mild shocks where the velocity field is “rough” (turbulent).

Grinstein, Magolin & Rider (2007) stressed the importance of shocks in ILES. At the zone level, we solve the Riemann problem by a shock-capturing algorithm, the piecewise parabolic method (PPM) of Colella & Woodward 1984; Woodward 2007; Leveque 2002⁴.

The “effective numerical viscosity” of PPM has been shown (Sytine, et al. 2000; Woodward 2007; Porter & Woodward 2007; Kritsuk, et al. 2011) to be much smaller, for the same number of zones, than for a pseudo-viscous method or a direct numerical simulation (DNS); i.e., ~ 4 times higher Reynolds number.⁵ DNS and our ILES converge to the same limit with zone refinement (Sytine, et al. 2000). Had it been available when we began, the piecewise parabolic boltzmann scheme (PPB) might have allowed an additional factor of 3 reduction in numerical dissipation (Woodward 2006). However, the insensitivity of our overall dissipation to our zoning suggests that this would make no qualitative difference in the results reported here.

2.1.2. Emergent dissipation and “Blowup”

Viscosity smooths gradients of velocity; shocks have an opposite tendency. Shocks imply discontinuities, a consequence of the nonlinearity of the compressible fluid dynamics equations (Landau & Lifshitz 1959). Shocks convert some of their kinetic energy into internal energy, a dissipation process. This increases the sound speed behind the front, so that pressure waves can overtake it, accumulate, and steepen the gradients there. While the

³ The shock jump conditions provide a dissipation independent of viscosity.

⁴ The pioneering work by Paul Woodward and his collaborators is not widely known in the solar literature; see however Porter, Anderson & Woodward (1997); Porter & Woodward (2000, 2007); Woodward (2007); Sytine, et al. (2000); Woodward et al., (2009). We thank Woodward for providing access to unpublished results which preceded and paralleled ours.

⁵ Most dissipation in PPM for Euler equations is provided by “flattening”, to eliminate oscillation behind shocks (monotonicity). There can still be small errors behind some strong shocks (“ ~ 0.03 in density, which disappear downstream”). A small amount of additional dissipation may then be needed, ≤ 0.1 of that required for “stabilization”. In this sense our ILES are “inviscid”. See Colella & Woodward (1984).

¹ See Meakin & Arnett (2007a,b); Arnett, Meakin & Young (2009); Viallet, et al. (2013); Mocák, et al. (2014); Arnett, et al. (2015); Cristini, et al. (2017, 2019); Arnett, et al (2019), and references therein.

² “Weak solutions” allow surfaces of discontinuity, such as shocks.

internal structure of the front is affected by the dissipation mechanism, the jump conditions and total dissipation are not.

As the inviscid limit is approached in a compressible turbulent medium, viscosity is less able to smooth gradients, so that shocks develop. Formally, shocks have infinite gradients of velocity at the front; these could be smoothed by viscosity, real or numerical, or replaced by the shock jump conditions. The Euler equations can develop singularities in a finite time, a phenomena that is sometimes termed “blowup” (Frisch 1995; Hoffman & Johnson 2008; Benzi & Frisch 2010). Our numerical version of the Euler equations also develops singularities (shocks). Shock capture could be approximated by an appropriate laplacian viscosity term if desired. However our method gives a physically correct dissipation at the grid level (e.g., §2.4, §3.1, §4), with fewer zones required.

As a gradient in velocity grows, PPM replaces the developing discontinuities by a nonlinear solution of the Riemann problem at the grid level, regularizing the simulations, and providing local support. Here “local support” implies monotonicity, i.e., no ringing at discontinuities (Gibbs phenomena); such errors plague both Fourier and high order polynomial methods of fluid dynamics.

To resolve dissipation in the incompressible NS equations, the computational zone size is constrained by viscosity (Pope 2000). For compressible flow, the Euler equations support shocks, so dissipation can occur by microscopic processes in the shock front, where gradients are large but the width of the shock can be small. P. Johnson (2021a,b) has shown that strain-rate self-amplification (shocks) are a major mechanism of energy transfer from large to small scales in turbulence. Replacing a shock by jump conditions allows us to *capture dissipation without resolving shock structure*, avoiding the linear size restriction of DNS for high Re (Pope 2000).

At low viscosity (high Re), almost identical initial velocities can evolve on different paths, a behavior characteristic of turbulence. In our view this is not due to “incorrect” initial conditions, but to *insufficient dissipation to keep close trajectories from developing steep velocity gradients (shocks)*. A similar problem arises with a Fourier representation of the velocity field by a finite number of frequencies.

In our ILES, shock structure is replaced by a discontinuity between two zones, so in this sense our algorithm minimizes the number of zones required. Microscopic details of shock structure are replaced by macroscopic discontinuities (Landau & Lifshitz 1959), allowing *fluid dissipation with no explicit viscosity*. This does not mean that microscopic dissipation does not happen (it

does in the narrow shock front), only that *we need not resolve it. It is globally constrained by the Euler equations*.

Even for mild convection (down to Mach numbers as small as 0.01, which we simulate), shocks give dissipation in our ILES. For lower Mach numbers, which we do not simulate, other mechanisms are available (Taylor 1937; Onsager 1949; Batchelor 1960; Hoffman & Johnson 2008; P. Johnson 2021a). We do not attempt to determine this transition precisely. Dissipation is not simply a microscopic phenomenon, but an emergent feature of the nonlinear advection term which is common to the Euler and NS equations (§3.4).

Turbulence gives a multi-scale behaviour which allows shocks to regularize our ILES. This kind of “coarse grained” approach is appropriate to stellar physics. It allows us to use “generalized” Euler equations, with a dissipative anomaly for TKE (Onsager 1949) to give the rate of energy flow in the turbulent cascade. Dissipation results from the Euler equations themselves, and can be described by Reynolds stresses generated by flows associated with the advection term (§3.4.1, §4).

Alternatively, Eyink & Drivas (2018a,b) have discussed these same points (and more) in a non-perturbative renormalization group analysis of the compressible NS equations, a very different viewpoint. Their more general approach gives interesting parallels (Eyink 2018) to our discussion, and the encouragement of no obvious contradictions.

2.2. The Reynolds number

Turbulent flows are classified by a dimensionless ratio, the Reynolds number, $\text{Re} = \ell \Delta u / \nu_{\text{NS}}$. Large ℓ gives large Re and extreme turbulence, provided that atomic-scale collisions are frequent enough for the fluid approximation to be valid, which is generally true in stars. If we use the Euler equations, for which $\nu \equiv \nu_{\text{NS}} \equiv 0$ so $\text{Re} \rightarrow \infty$, how do we define a Reynolds number?

Landau & Lifshitz (1959) in their Eq. 32.6 express Re as

$$\text{Re} \sim (\ell / \lambda_0)^{\frac{4}{3}}, \quad (1)$$

for $\ell \gg \lambda_0$, so Re is a measure of the ratio of the integral length scale ℓ (largest eddies) to an internal scale λ_0 (smallest eddies as defined by a dissipation scale); see also Warhaft (2002).

Shocks are a collective nonlinear behavior. With shocks the effective dissipation scale is the shock thickness. The grid scale is the zone size Δr , which is also the effective dissipation scale for the shock-capture algorithm in our ILES. If $\Delta r \gg \lambda_0$, shock capture allows dissipation to be realistically simulated for systems much

larger than the shock thickness, for the same computational Re constraint (number of zones).

An effective Reynolds number Re^* can be determined by the available zoning, rather than a microscopic viscosity. Finer zoning allows smaller effective viscosities (i.e., reduces gradients) and so permits larger Reynolds numbers. A general calibration of Re^* relative to Re is nontrivial (Landau & Lifshitz 1959, §32; Haugen & Brandenburg 2006). A useful approximation at large Re for our problem is

$$Re^* \sim (n/2)^{\frac{4}{3}}, \quad (2)$$

where $n/2$ is the number of computational cells across the turbulent domain in our n^3 simulation. This is easily evaluated for both Euler simulations (which have a prefactor of order unity) and NS simulations (which have a prefactor about 4 times smaller, assuming that the NS algorithm uses 4 zones to deal with shocks).

As long as the physical shock thickness is much less than the zone size, the shock jump conditions are a physically correct dissipation mechanism, so this is a promising approach to fluid flow for large scales (large Re).

In our ILES the range of n is 128 to 1536 so that the estimate of Re^* ranges from 256 to 7×10^3 . The morphology of the simulations can be bracketed by photographs of experiments which are identified with Reynolds numbers. We approach the “mixing transition” at $Re \sim 10^4$ of Dimotakis (2005), who presents flows in this range (his Fig. 1 gives Re of 1.75×10^3 to 2.3×10^4 , and Fig. 2 gives Re of 2.5×10^3 to 1.0×10^4). See also Van Dyke (1982). Thus $Re \approx Re^*$ (for $Re^* \gg 1$).⁶

Early experiments established that solutions to the NS equations possessed a Reynolds-number similarity: if the values of Re are the same then the scaled flows are the same. The Euler equations are invariant with respect to scale transformations in ℓ , u , and mass density ρ (Pope 2000), and represent the inviscid limit of the NS equations. Having small size relative to stars, laboratory-scale turbulence is strongly affected by finite ν_{NS} in the Navier-Stokes equations (Batchelor 1960).

2.2.1. ILES results

Paper I (Arnett, et al 2019) is accompanied by movies of (i) the evolution in time (“Very high resolution movie of the C-shell”), and of (ii) a fly-through of the computations at a given instant in time (“Carbon shell (1024³)

simulation: fly-through movie”)⁷. The simulations are approaching a statistical steady state in time, and statistical homogeneity in space, as the similar visual appearance of the movie and the fly-through suggests.

Our ILES allow us to separately monitor the conservation of turbulent kinetic energy (TKE), which is not conserved (it dissipates to become internal energy), and the conservation of total energy, which is almost exactly conserved in our simulations. This allows us to directly measure dissipation due to nonlinear fluid effects (P. Johnson 2021a). Multiple runs with different grids allow us to probe the dissipation rate and the TKE spectra with changing resolution.

Fig. 1 shows the complex filamentary structure that develops in ILES of the turbulent velocity field (Cristini, et al. 2017, 2019); the magnitude of velocity is shown for a cross-section of the C+C burning shell. This is frame 138 from the movie; these contours of velocity magnitude show “roughness” (Tennekes & Lumley 1972; Onsager 1949). Turbulence appears in patches in space-time, a feature associated with an anomalous behavior: intermittency.

The initial state was a relaxed model mapped from a 512^3 onto a 1024^3 grid. The first steps at increased resolution show changes at the smallest scales first, as expected, which then work up to the largest scales. We find that the “texture” of the velocity field becomes *finer rather than smeared*, and above the grid scale sharp gradients are maintained ($\theta \leq \frac{1}{3}$, §2.1.1).

The top and bottom regions support waves and are in a quasi-steady state. At the fluid boundaries these waves connect to nonlinear solutions of the Riemann problem, giving monotonic support for shocks and rarefactions (Hölder continuity). These arise naturally in high Re turbulence ($\theta \leq \frac{1}{3}$, middle layer). We have horizontal wave-damping layers at the distant edge of the grid (Meakin & Arnett 2007b) to avoid reflections. Similarly, radial waves are not reflected. The bottom layer is also a domain where waves dominate, but its higher density gives lower amplitude waves, which are barely visible with this choice of color palatte. The wave domains and turbulent regions are separated by thin boundary layers which develop naturally (blue arrows in Fig. 1).

Our sequence of ILES have changes only in resolution (Cristini, et al. 2017; Arnett, et al 2019). Like Onsager (1949), we find a rapid convergence to a cascade. The

⁶ We find that the critical values of Re^* for *onset of turbulence* tend to be lower than Re for some common engineering cases, possibly because of fluid-fluid boundaries in stars, or our use of the Euler equations.

⁷ The time evolution and the fly-through movies may be found at <http://www.astro.keele.ac.uk/shyne/321D/convection-and-convective-boundary-mixing/visualisations>.

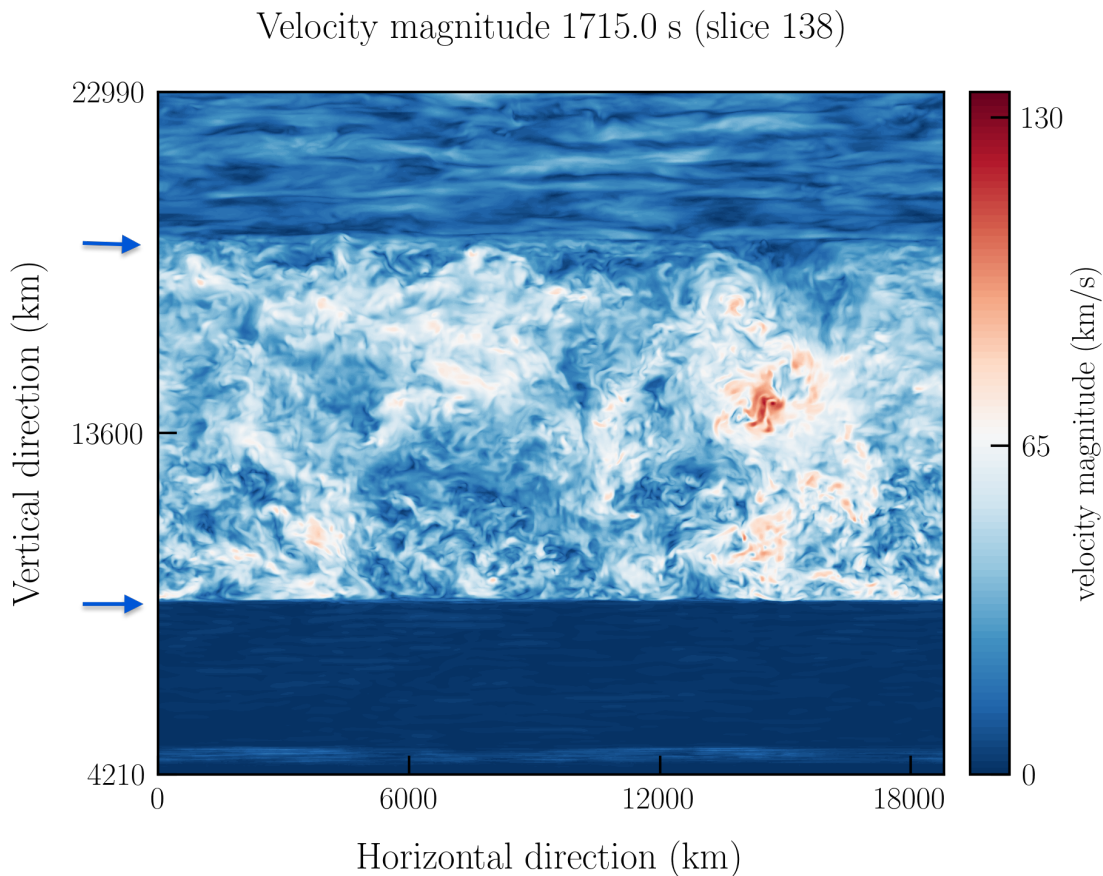


Figure 1. Vertical slice of velocity magnitude (Mach ~ 0.02) from a compressible Euler simulation (using PROMPI), of a C+C burning shell (after 1024^3 case in Cristini, et al. 2019 and Fig. 1, Arnett, et al 2019). According to Eq. 2, this $Re^* \sim 6000$ (compare to Fig. 2 in Dimotakis 2005). Weak pressure waves propagate, and steep gradients are captured by a Riemann solver (PPM, §2.2.1). This is a typical frame from the movie at time $t = 1715$ s (slice 138). Blue arrows at left axis point to sharply defined top and bottom boundary layers, which form naturally and support surface waves. Here Onsager’s $\theta = 1/3$ implies a singularity in the u gradient. The top and bottom edges of the grid are beyond the edges of the figure. Wave motion is noticeable above the top boundary layer; a distant damping layer prevents reflection of waves back into the convective region. The velocity field shows filamentary fine structure (“roughness”) due to the turbulent cascade, as well as coherent structures (rolls and plumes) which form and dissolve. Intermittency is suggested in this snapshot, and is obvious in the movies. On average smaller scale structures are weaker and evolve faster, but occasionally large scale structures are torn apart by powerful mutual interactions.

energy is contained by a few modes of low-order.⁸ These results agree with Holmes, Lumley & Berkooz (1996), who stress the importance of low order modes to the energy-containing scales of turbulence (see their Chapter 3).

2.3. Navier-Stokes methods

2.3.1. DNS

In contrast to ILES,⁹ direct numerical simulation (DNS) uses the NS equations and attempts to simulate all relevant scales of that flow; it is the standard against which other methods are compared in the fluid dynamics and applied mathematics communities.

DNS usually involves incompressible flow and molecular dissipation. For astrophysical scales these assumptions become untenable. The ratio of the NS dissipation to the other (Euler) terms scales as $1/\text{Re}$; see §A. For large Re , other (nonlinear) dissipation mechanisms will dominate (§2.1.2); this is the case for stars. The standard theoretical framework (e.g., based on Batchelor 1960; Pope 2000), requires modification in this limit. For standard DNS of turbulence, most of the computational effort (>99% according to Pope (2000), p. 357, §9) is used to resolve the small scales, i.e., the Kolmogorov dissipation scale (Tennekes & Lumley 1972; Pope 2000), $\eta = (\nu_{\text{NS}}^3/\epsilon)^{1/4}$, where ν_{NS} is the kinematic viscosity and ϵ is the effective rate of turbulent dissipation per unit mass. This leaves correspondingly few computational resources for the large scales, which contain most of the energy and drive the flow, or for longer temporal evolution, which is vital for statistics. Despite these constraints, high resolution DNS are a useful theoretical check for astrophysical problems.

Experiments (Warhaft 2002) and high resolution DNS (Sreenivasan 2019; Falkovich & Sreenivasan 2006) demand features beyond those in the standard picture of Kolmogorov (1941). The DNS of Iyer, et al. (2018), have a Taylor-scale Re of 650 using a 4096^3 grid, and show a “ramp-cliff” structure in turbulent velocity u , with ramps being relatively placid regions between cliffs. Following Iyer, et al. (2018), who find that “the scalar

intermittency is dominated by the most singular shock-like cliffs in the scalar field,” *we interpret these cliffs as shocks* (§2.1.2). A strict DNS approach would require that these shocks be resolved after viscous spreading on the grid, taking multiple zones per shock, as did Iyer, et al. (2018).

2.3.2. LES

A less demanding class of computational options, the large eddy simulations (LES) of the NS equations¹⁰, do not attempt to resolve the details of dissipation. For a given number of zones this allows larger length scales to be simulated, at the expense of approximation errors in the dissipation rate and turbulent cascade (§2.4).

We discuss only two of the many options: (i) a Smagorinsky pseudo-viscosity for shock capture (Haugen & Brandenburg 2006; Pope 2000), and (ii) hyperviscosity stabilization (Haugen & Brandenburg 2006; Kritsuk, et al. 2011; Stein, Nordlund & Kuhn 1989b).

To avoid numerical issues with shocks, an artificially large viscosity (small Re) is adopted to smooth any sharp front in velocity. This converts kinetic energy into internal energy (Fig. 12.3 & 12.4, Richtmeyer & Morton 1967). Usually several zones are required for the pseudo-viscous representation of a shock. To obtain an average of the turbulent behavior, space-time integrations over representative volumes of space and several turn-over times are needed.

The hyperviscosity method of Stein & Nordlund (1989) is different. They note: “Since this is compressible flow, shocks can form. *These instabilities are removed and the code is stabilized by applying artificial diffusion to all the fluid equations.*” This seems to mean that artificial diffusion is increased (Re decreased) until the flow is “stabilized”, i.e., *no longer turbulent*, but laminar. This is then used to approximate the space-time average of a turbulent flow.

Turbulence is a physical instability, not a numerical artifact, so arbitrary damping may have unintended consequences (§6.2).

Due to the conflation of artificial viscosity with nonlinear fluid dynamics, LES do not provide a clear estimate of turbulent driving and damping, as we present for ILES (§3, §4, §5). Eq. 2 may then *overestimate* the effective Re .

2.4. Specific TKE spectra¹¹

⁸ For the O+O shell (§4.1), the lowest mode has ~ 45 percent of the turbulent energy, with ~ 75 percent in lowest 4 modes, during the 400 s examined by Meakin & Arnett (2007b). The C+C shell (§4.2) is simpler, with no significant ingestion of a new fuel and the lowest 3 modes dominate.

⁹ Our ILES grid need extend only from the integral scale ℓ down to a size where the total dissipation by shocks in the turbulent cascade is captured (our grid scale Δr), not to a Kolmogorov molecular dissipation scale η as usually assumed in DNS (see Fig. 2). This requires no changes in our code, only in our interpretation. This extends the incompressible picture of the cascade (Taylor 1937; Batchelor 1960) to compressible flow.

¹⁰ We follow the terminology of Pope (2000).

¹¹ We agree with Kritsuk, et al. (2011) that we should not attempt a serial ordering of quality for well tested numerical codes used to attack a variety of multi-faceted problems. Our method may have some advantages for turbulence study.

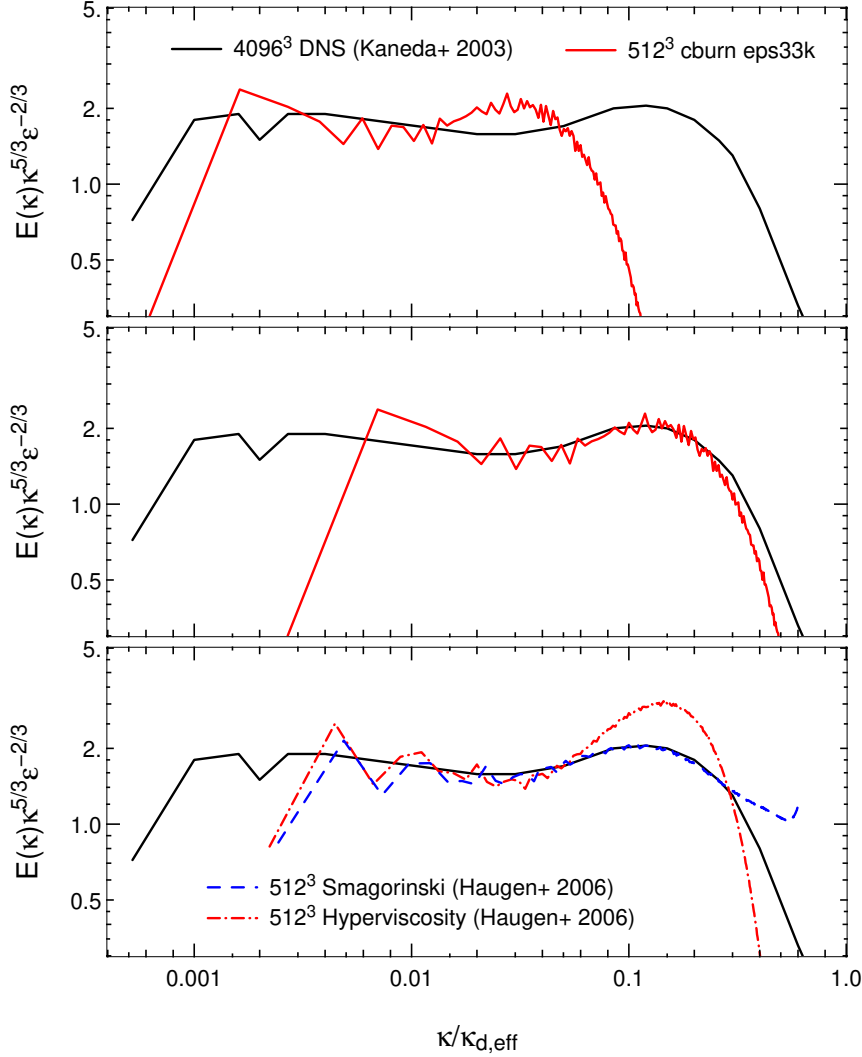


Figure 2. Cascades: spectra of specific kinetic energy (after Fig. 1, Haugen & Brandenburg 2006). **(Top)** DNS showing a reference solution (4096^3 , $Re=1201$, NS equations) from the Earth simulator (solid line, Kaneda, et al 2003), and Euler ILES (PROMPI, Cristini, et al. 2019, Fig. C1, with a 512^3 grid, $Re^* \sim 1600$ from Eq. 2). The spectra are “compensated” so that the inertial range is horizontal. The integral scale (the energy-containing eddies) lies at the left end of the curves, and the dissipation range at the right end. The DNS and the **(red)** eps33k ILES (high luminosity boost) spectra are in a quasi-steady state. The “molecular” dissipation scale is the Kolmogorov scale η , (where $\eta^4 = \nu_{NS}^3/\epsilon$). For stars this is small, formally lying far beyond the right end of the ILES curve, so that *physical dissipation is dominated by shocks, independent of viscous parameters*, adjusting to whatever heating rate is imposed (§3.1). The effective dissipation scale is resolved; it is much larger than the width of the simulated shock, i.e., the width of a zone. For the converged DNS the dissipation scale is also resolved, but using the NS viscosity, which could be reasonable for laboratory scales. **(Middle)** Same as **(Top)**, except ILES is shifted to the right so the dissipation ranges may be compared. The solid curve in the dissipation region of the benchmark DNS (Kaneda, et al 2003) matches our ILES (Cristini, et al. 2019) surprisingly well, despite very different physical mechanisms and mildly different Re . DNS and ILES seem to converge to the same limit for high Re ; see also Porter & Woodward (2007). The ILES dissipation is insensitive to zoning, from grids of 128^3 to 1024^3 . The ILES inertial range lengthens with finer zoning. **(Bottom)** Same as **(Middle)**, but replacing the (red) ILES spectrum with two spectra from Haugen & Brandenburg (2006) of 512^3 LES spectra of the NS equations, which are also shifted to the right. The hyperviscosity (red dash-dotted line) and the Smagorinsky viscosity (blue dashed line) are normalized to the reference DNS by 1.1 and 0.95, corresponding to stronger and weaker dissipation than in the converged DNS reference (black solid line) or the ILES above. Hyperviscosity gives a distorted peak (the “bottleneck”) and an abruptly truncated spectrum, while the Smagorinsky pseudo-viscosity gives errors when approaching the grid scales. DNS and ILES are similar in decrease at high wave-number.

On average in our ILES, the turbulent kinetic energy flows in a cascade with a Kolmogorov-like spectrum, beginning at the integral scale ℓ and ending at the effective dissipation scale, which is at the resolution of our simulations (the grid scale). Our presentation was inspired by Fig. 1 in [Haugen & Brandenburg \(2006\)](#). We place our ILES in context by examining spectra of specific turbulent kinetic energy (TKE) in Fig. 2. The spectra are scaled so that the inertial range becomes a horizontal line, which connects the energy containing eddies (the integral scale) at the left end of the curve, to the dissipation range at the right end. The inertial range is supposed to be a conduit for TKE, with the physics of acceleration contained in the integral scale and the physics of damping in the dissipation range. We can evaluate each from our ILES.

Shocks are 3D objects, having a microscopic dimension across the front, and two macroscopic dimensions defining a surface. In turbulence, interacting shocks provide communication between large and small scales, and thus contribute to Fig. 2 in multiple places. In the oversimplified picture of the classical cascade, a turbulent “patch” has a single wavelength; it would be created on the left, propagate through the inertial range, to be dissipated on the right in the dissipation range. Instead we find a “leaky” conduit ([P. Johnson 2021a](#)), where interacting shocks can affect both large and small scales at once, and “accelerate” the dissipation as required ([Onsager 1949](#)).

Such a construction necessarily favors intermittency; the separation of scales for driving and damping make synchronization impossible. The mechanisms also can differ for different problems, e.g., damping can be due to molecular collisions, shocks, plasma damping, or charge separation in collisionless plasma, suggesting relevance to a range of topics from cosmic-ray acceleration to generation of bursts of radio noise.

All panels show a benchmark DNS (solid black line) of 4096^3 zones ([Kaneda, etal 2003](#)) with no magnetic field¹². This benchmark is a converged DNS of the NS equations, which represents the solution to which all correct NS algorithms converge for this Re. Eq. 2 gives an estimated Reynolds number of $Re^* \sim 1600$ for the 512^3 grid of our ILES, which is slightly less viscous than the Taylor microscale $Re \sim 1201$ for [Kaneda, etal \(2003\)](#), which our energy spectrum resembles.

The top panel compares the Kaneda DNS to our ILES for a 512^3 grid with boosted heating (eps33k, red line). The largest length scales are at the left, and differ because the boundary conditions differ slightly between DNS and ILES. The very largest eddies show strong fluctuations which are slow to average out. The eps33k (red) case relaxes to establish an inertial range, which does not extend so far to the right as the Kaneda case because the coarser grid has larger zones (512^3 vs. 4096^3). The dissipation scale occurs where turbulent kinetic energy is converted into internal energy, and its position depends upon the mechanism which makes that conversion. Dissipation is less efficient for molecular collisions (DNS) spread over a uniform medium (the Kolmogorov scale) than for shock dissipation (ILES) occurring in a thin front, so the DNS requires more inertial range between the integral scale and the dissipation scale for this range of Re, as shown.

The middle panel differs from the top panel only in a horizontal shift of our ILES, made to aid comparison of dissipation regions. It is interesting how well the shape of DNS dissipation (due to molecular viscosity) agrees with that of ILES dissipation (due to shocks), considering the different mechanisms invoked. The implied length scales differ by orders of magnitude, from molecular viscosity scales for NS equations to computational zone size (shock width) for the Euler equations. The turbulent cascade develops whatever dissipation rate is needed. Use of the shock jump conditions means that the computation need not resolve the physical shock structure, and supports our horizontal shift through the neutral inertial range (the “cascade”).

The bottom panel compares DNS to two lower resolution solutions of the NS equations, hyperviscosity LES (red dot-dashed line) and Smagorinsky LES (blue dashed line), both with 512^3 zones and no magnetic field ([Brandenburg \(2016\)](#)). The two LES are normalized to the DNS results. Horizontal shifts were performed as in the middle panel. We expect the hyperviscosity case to be indicative of the STAGGER code ([Stein & Nordlund 1989](#); [Stein, Nordlund & Kuhn 1989b](#)).

The hyperviscosity LES show a “bottleneck” feature, which is larger than for DNS, ILES, or Smagorinsky LES. The hyperviscosity LES has more dissipation; see also [Porter & Woodward 2007](#), Fig. 7.2 and 7.3. This bump (near scaled wavenumber 0.1), is due to a design choice: the higher viscosity required for the abrupt termination of the cascade. To the right of this bump the hyperviscosity spectrum gives a corresponding error of opposite sign, a deficit of short wavelength motion prior to that cutoff.

¹² Traditionally magnetic fields are ignored deep in stellar interiors because of their relatively low energy densities. With significant rotation and turbulence this approximation should be re-examined; magnetic fields can resist shear and amplify ([Parker 1979](#)). The predicted turbulent spectrum (Fig. 2) may affect this.

The hyperviscosity LES is sixth order in space and third order in time. As we have emphasized in §2.1.2, turbulent velocities (and shocks) are not well represented by high order polynomials. The piecewise cubic representation of our ILES is better suited to a Hölder continuous flow (§2.1.1). The combination of a higher order dissipation and a sharp cutoff at the grid scale probably enhance the bottleneck error (Haugen & Brandenburg 2006) by approximating shocks by a high order polynomial (Fig. 2).

The Smagorinsky LES shows an opposite tendency, a slower fall at high wavenumber than the benchmark DNS, which is attributed to “strongly nonlocal interactions in wavenumber space”, and is likely to be related to the choice of pseudo-viscosity.

The bottleneck becomes smaller with finer resolution in both DNS and ILES (Porter & Woodward 2007). It is striking that a 512^3 ILES can resemble a 4096^3 DNS in many respects (Fig. 2), despite 1/8th as many zones per coordinate; see also §2.3.1.

3. DYNAMICS OF THE TURBULENT CASCADE

The rate of turbulent dissipation ϵ is not uniform in space and time in our ILES, but must balance driving on average.

3.1. Global damping

Based upon the assumption of universality of isotropy at small scales, Kolmogorov (1941) derived an average value for the rate of dissipation over the cascade,

$$\langle \bar{\epsilon} \rangle \sim (\Delta u)^3 / \ell_d, \quad (3)$$

where Δu is the velocity scale of the largest eddies and ℓ_d the damping length for TKE (roughly the size of the turbulent region). The angle brackets denote a spatial average over the turbulent region, and the overline a temporal average over several turnover times. Onsager (1949) has commented that Eq. 3 was independently derived at least twice. For a review of Eq. 3, see Vassilicous (2015).

Do not confuse the average property of the global flow, ℓ_d , long established experimentally as a global feature of turbulence (Batchelor 1960, §6.1), with the Kolmogorov scale, η , which is local, based on molecular viscosity. Always $\ell_d \gg \eta$. The average rate of dissipation $\langle \bar{\epsilon} \rangle$ is determined by ℓ_d , which depends on (i) the flow structure, and (ii) the velocity scale of the largest eddies Δu . In contrast $\eta = (\nu_{\text{NS}}^3 / \epsilon)^{1/4}$ is an estimate of the scale at which a NS molecular viscous dissipation would smooth the flow (Fig. 2). For DNS, these are separated by the inertial range (Batchelor 1960), with an η which depends

on the NS viscosity, and goes to 0 as $1/\text{Re}$ does for inviscid flow. For ILES the size of the smallest possible eddy is the grid scale, which is always finite.

According to Kolmogorov¹³, the cascade proceeds down to smaller scale eddies, losing information about the large scale structure of the flow, according to

$$\langle \bar{\epsilon} \rangle \sim (v_\lambda)^3 / \lambda, \quad (4)$$

where $v_\lambda = u - \bar{u}$ for each eddy size $\lambda \leq \ell$ (Landau & Lifshitz 1959, §31). The turbulent kinetic energy is assumed to flow to smaller scales through each level of the cascade (Batchelor 1960), down to the dissipation range.

Instead (in Paper I and Arnett, Meakin & Young 2009), we find lumpy, intermittent dissipation, shocks, and direct interactions between large and small scales of the flow, although *the average value of the rate of dissipation* $\langle \bar{\epsilon} \rangle$ is similar to Eq. 3. We find $(\Delta u)^3 \sim u_{\text{rms}}^3$, where u is the turbulent velocity. Arnett, Meakin & Young 2009 found (their Fig. 2),

$$\langle \overline{\epsilon_{\text{nuc}}} \rangle \approx \overline{u_{\text{rms}}^3} / \ell_d, \quad (5)$$

where ℓ_d defines a *global damping length for turbulent kinetic energy*, and ϵ_{nuc} is the nuclear heating which drives the convective shell, so $\langle \overline{\epsilon_{\text{nuc}}} \rangle = \langle \bar{\epsilon} \rangle$. This is similar to Eq. 6.1.1 in (Batchelor 1960), with the empirical scaling factor, $A \approx 1$. Eq. 5 gives the value of the TKE dissipative anomaly, the flux of TKE in the cascade, and a specific scaling for total energy conservation in Fig. 2.

3.2. Acceleration of the cascade

Onsager (1949) suggested that cascade redistribution of energy proceeds by steps typically in a geometric series, by a factor of order $\frac{1}{2}$ per step. *The first few steps in the cascade limit the over-all speed of the process*, which means that “subsequent steps must be accelerated”. The actual first stages are complicated, but our ILES treats them without problem. The subsequent stages occur quickly, supporting Onsager’s picture. If no other process intervenes, shocks will develop on a sonic time scale to provide whatever dissipation is necessary for the cascade (§2.1.2). *There is no need to resolve the scales of molecular viscosity with our ILES.*

There is a subtle question here of energy flow versus energy content. Eyink (2018) quotes Landau & Lifshitz 1959, §31: “We therefore conclude that, for the large eddies which are the basis of any turbulent flow, the viscosity is unimportant and may be equated to zero, so that the motion of these eddies obeys Euler’s equation.

¹³ However see P. Johnson (2021a) on “leaky” cascades.

In particular, it follows from this that there is no appreciable dissipation of energy in the large eddies.” Eyink (2018) suggests: “The latter statement is only true, however, for the direct viscous dissipation of kinetic energy at inertial-range scales, whereas the energy in eddies at those scales, in fact, must be dissipated. The rate of decrease of energy for free-decay or rate of power-input for forced turbulence are objective facts that cannot depend upon the resolution of eddies in the inertial-range.” The energy cascade is in a steady state if flow in from larger scales is balanced by flow out to smaller scales, with no accumulation.

Eyink (2018) explicitly writes the coarse-grained Euler equations plus the anomaly (“an energy flux from deformation work of the large-scale strain against the small scale stresses”). The mechanism of TKE loss is just the energy cascade (Onsager 1949), and also applies to our ILES of the Euler equations (§3.4.1). At these large scales the TKE is not thermalized (yet) but flows “away from our notice” to smaller scales (Fig. 2 and §2.4).

Our ILES form such a turbulent cascade, generated at the integral scale. This TKE cascades down through the inertial range, to the dissipation range (our grid scale). Our methods allow us to monitor the average dissipation due to the Riemann solver, which will be shown in §4. This is the nonconservation of TKE for ($\theta \leq 1/3$) discussed by Onsager (§2.1.1). *This dissipation of TKE is not controlled by an imposed parameter, but a self-consistent result of the ILES of the Euler equations, which implicitly constrain the flow.*

The ILES develop a cascade which we find to dissipate at the rate that Kolmogorov derived assuming local isotropy for turbulence (Eq. 5). However, like results from experiment (Warhaft 2002) and DNS (Sreenivasan 2019; Iyer, et al. 2018), our ILES have an “anomalous” higher order behavior. Our previous interpretation of our numerical results is subtly altered and strengthened. Further research is needed to precisely determine the degree of overlap between DNS and ILES methods.

3.3. Time dependent Böhm-Vitense theory (MLT)

To better understand turbulent time dependence, and to connect to stellar evolutionary calculations, we consider the familiar and simpler MLT. MLT is inconsistent: it assumes flow, but is a local theory. It artfully averages over a “mixing length” to deal with this problem. This makes comparison with 3D ILES conceptually challenging. We replace the algebraic formulation (Biermann 1925; Böhm-Vitense 1958) with a differential equation (Arnett 1968), using Böhm-Vitense’s estimate of driving \mathcal{B}^{bv} , and damping $\mathcal{D}^{bv} = v|v|/\ell_d$ from §3.1

(the relaxation timescale is $\ell_d/|v|$), so

$$dv/dt = \mathcal{B}^{bv} - \mathcal{D}^{bv}, \quad (6)$$

where v is the flow speed and ℓ_d the MLT mixing length, which is directly related to dissipation length. If we multiply this equation by v we obtain a primitive TKE equation. In a hypothetical quasi-steady state (MLT), we would have

$$\langle \overline{\mathcal{B}^{bv}} \rangle \sim \langle \overline{\mathcal{D}^{bv}} \rangle, \quad (7)$$

which is the simplest version of the “dynamic constraint” (§2.1.1). While \mathcal{B}^{bv} is local, \mathcal{D}^{bv} is a property of the turbulent cascade, so they represent different length scales, and can not remain in phase. Unless \mathcal{B}^{bv} and \mathcal{D}^{bv} are in phase, Eq. 6 has dynamic solutions which must be averaged. This demands intermittency (Tennekes & Lumley 1972), not as a superficial feature, but as necessary for the existence of a quasi-steady state in both this simple and in more realistic convection models.

In MLT,

$$\langle \overline{\mathcal{B}^{bv}} \rangle \equiv \langle \overline{g\beta_T\Delta\nabla} \rangle, \quad (8)$$

where g is the gravitational acceleration, $\Delta\nabla = \nabla - \nabla_e$ is the super-adiabatic excess, and β_T is the thermal expansion coefficient (Kippenhahn & Weigert 1990). The entropy excess $\Delta\nabla$ may contain contributions from composition differences, which are ignored in MLT, but are required at boundaries of evolving stars. To evaluate these, the problem of mixing must be solved consistently with that of convection (Arnett, et al. 2015; Woodward et al. 2015; Mocák, et al. 2018).

3.4. TKE equation

Some of the behavior in our library of 3D ILES can be captured with a more general turbulent kinetic energy (TKE) equation (Meakin & Arnett 2007b; Mocák, et al. 2018; Arnett, et al 2019), which we improve here to include insights from Onsager (1949).

Using (i) the momentum conservation equation for turbulent flow in a hydrostatic background, (ii) the mass conservation equation, and (iii) taking a dot product with the velocity fluctuation \mathbf{u}' relative to a co-moving frame (Arnett, et al 2019), gives a turbulent kinetic energy (TKE) equation (compare Eq. 6),

$$D_t(\rho\mathbf{u}' \cdot \mathbf{u}'/2) = -\mathbf{u}' \cdot \nabla P' + \rho'\mathbf{u}' \cdot \mathbf{g} \quad (9)$$

where the primes denote turbulent fluctuations. The left-hand side is a co-moving time derivative.

Taking averages and requiring $\langle \rho'\mathbf{u}' \cdot \mathbf{g} \rangle \rightarrow 0$ in order to remain in the comoving frame after fluctuations,

$$\langle \overline{D_t(\rho\mathbf{u}' \cdot \mathbf{u}'/2)} \rangle = -\langle \overline{\mathbf{u}' \cdot \nabla P'} \rangle \quad (10)$$

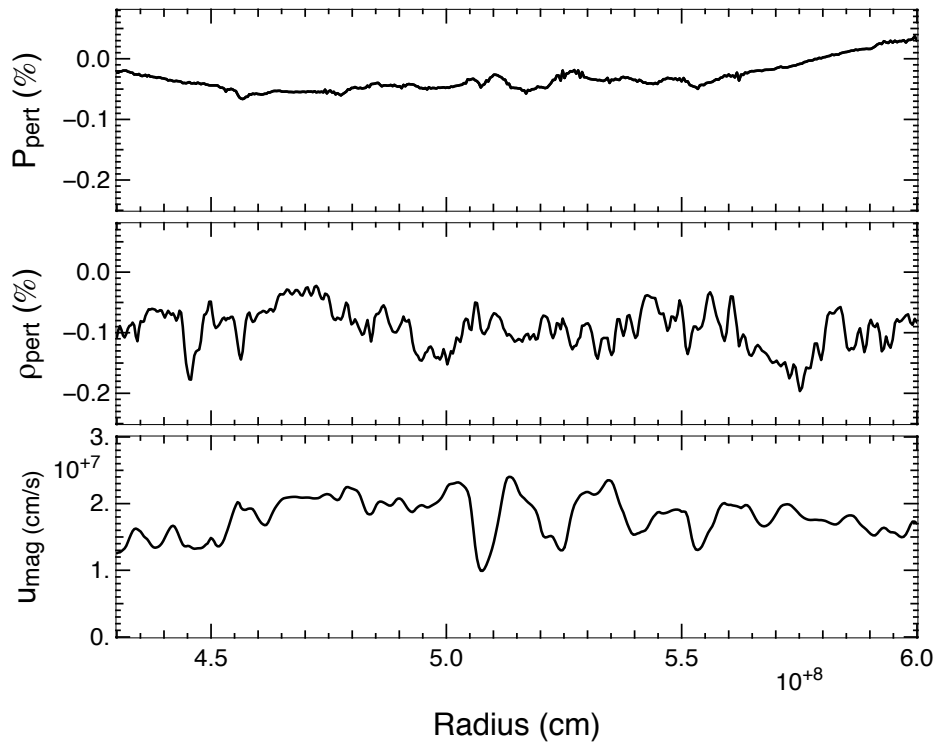


Figure 3. (Top) pressure fluctuations, (Middle) density fluctuations, and (Bottom) turbulent velocity magnitude, all versus radius, from the interior of a PROMPI ILES of the O+O convective shell (Arnett, et al. 2015). These patterns suggest the presence of weak shocks. Pressure perturbations are weakened by expansion but the density perturbations are more robust, implying entropy perturbations also. The velocity structure is intermediate between these two, being “rough” at scales which are much smaller than the depth of the convective region (most of the convective region is shown; boundaries are omitted for simplicity). In our ILES, the PPM algorithm (Colella & Woodward 1984) applies “flattening” (i.e., “local support”) to suppress Gibbs ringing behind these weak shocks; this causes a “dissipative anomaly” to occur throughout the convective region, even with no viscosity (Onsager 1949).

3.4.1. Turbulent damping by Reynolds stress

In our ILES, *high-frequency oscillations in the turbulent velocity are responsible for a non-trivial Reynolds stress, giving a finite dissipation in the $Re \rightarrow \infty$ limit* (De Lellis & Sze’kelyhidi 2013). This corresponds to the domain of $\theta \leq \frac{1}{3}$ in §2.1.1, for which there is a thermalization of TKE by damping. Such convective velocity fluctuations are shown in Fig. 2 of Arnett, et al. (2015).

If we average $D_t(\rho \mathbf{u}' \cdot \mathbf{u}'/2)$ from Eq. 10 and assume a steady state, there is a residue in the $\theta \leq \frac{1}{3}$ region which is just the desired damping term $\rho \epsilon_K$ (see Eq. 5). We have

$$\rho \epsilon_K = \overline{\mathbf{u}' \cdot \nabla P'}$$
 (11)

but what is ϵ_K ?

This nonlinear mathematics is key to understanding turbulent cascades. The term is common to the Euler and NS equations, so they can converge to the same value in the inviscid limit.

The rate of increase in TKE is the product of an acceleration and a velocity, so

$$\mathbf{u} \cdot (\partial_t \mathbf{u} + \mathbf{u} \cdot \nabla \mathbf{u}) \rightarrow \partial_t u^2/2 + \partial_r u^3/3, \quad (12)$$

because the driving acceleration is parallel to gravity. For a quasi-steady state (a few turnover times), $\langle \partial_t u^2/2 \rangle \approx 0$, with a net cancelation. The other term is finite.

In the $\theta \leq \frac{1}{3}$ region we have “rough” (i.e., turbulent) flow. Fig. 3 shows the fluctuations of pressure, density and the velocity magnitude from the middle of the O+O burning shell from the Perth simulation (1536×1024^2) using PROMPI (Arnett, et al. 2015).

The fractional pressure perturbations are smaller than those for density; the density perturbations are less smooth, indicating significant entropy variations. The variations in turbulent velocity are indicated by velocity magnitude ($u_{mag} \equiv \sqrt{\mathbf{u} \cdot \mathbf{u}}$), which samples all three dimensions; this curve is smoother than the other two, but still “rough”, suggesting weak shocks (Mach \sim 0.05). For comparison, Fig. 1 shows a slice of velocity magnitude through the C+C shell.

This rough velocity field gives a residue from the $\partial_r u^3/3$ term which is robust against zoning error, being dominated by the largest scales; it varies little from 256^3 to 1024^3 grids (Cristini, et al. 2017, 2019; Arnett, et al. 2015). It is damped by “flattening”, which is consistent with a field of weak shocks spread over the convective region. As the amplitude of “roughness” increases, so does dissipation, giving negative feedback and a nonlinear bound to growth. Without this “flattening”, a wave would remain sinusoidal, conserving kinetic energy.

This is essentially the same physics, seen from a different viewpoint, as shown in Fig. 1 of Iyer, et al. (2018)

for a DNS realization using “molecular viscosity” for shocks, showing “ramp-and-cliff” structure (Sreenivasan 1979). DNS uses molecular viscosity to thermalize the post-shock regions, requiring several zones to span each shock (a cliff followed by a ramp is the simplest combination). ILES handles this more compactly.

Upon Reynolds averaging, the spatial derivative from Eq. 12 leaves a residue, which we evaluate numerically from our ILES. On average,

$$\epsilon_K = -\langle \overline{\partial_r (u^3/3)} \rangle \approx -\langle \overline{u_r^3} \rangle / \Delta_{cz}, \quad (13)$$

which is Eq. 5, and the turbulent damping length is $\ell_d \approx \Delta_{cz}$, the size of the turbulent region for weak stratification.

Arnett, Meakin & Young (2009) verified this numerically for weakly stratified convection (see their Fig. 2 caption). We numerically reconfirm it (Tables 1 and 2 in §4). Here we have obtained a similar result from our estimate of the Reynolds stresses in the turbulent flow (Eq. 13). This provides a normalization consistent with unity for our ILES in Fig. 2.

The TKE equation (Eq. 11) does not assume any particular flow or explicit dissipation (Meakin & Arnett 2007b). With weak stratification¹⁴ our ILES develop narrow downflows and broad upflows, but little net TKE flux due to significant up-down cancellation. The assumed symmetry of up-down flow in MLT requires the net flux of TKE to be zero, but finite TKE becomes necessary as increasing stratification further breaks symmetry.

This damping as a function of radius will be shown in detail in Fig. 5 and 6; its integral is the TKE anomaly (§2.1.1). For strong stratification we have an asymptotic value for the damping length, so Δ_{cz} is replaced by $\ell_d \sim H_\rho$ in Eq. 13; see §5.1.4.

3.4.2. Phase lags, driving and damping

Neutrino-cooled stages of burning are accessible to ILES (e.g., Meakin & Arnett 2007b; Arnett 1996). Deep convection in photon-cooled stages may be more challenging computationally because slower evolution is accompanied by flow at very low Mach number, giving subtle conservation law problems (Brown, Vasil & Zweibel 2012).

If we ignore the necessary phase lags between driving and damping, then on average in a volume segment of the turbulence we have Eq. 7, which is something like MLT (see Kippenhahn & Weigert 1990, Eq. 7.6).

¹⁴ Here “weak” means the depth of the convection region Δ_{cz} is no more than a few pressure scale heights. For “strong” stratification, see §5.

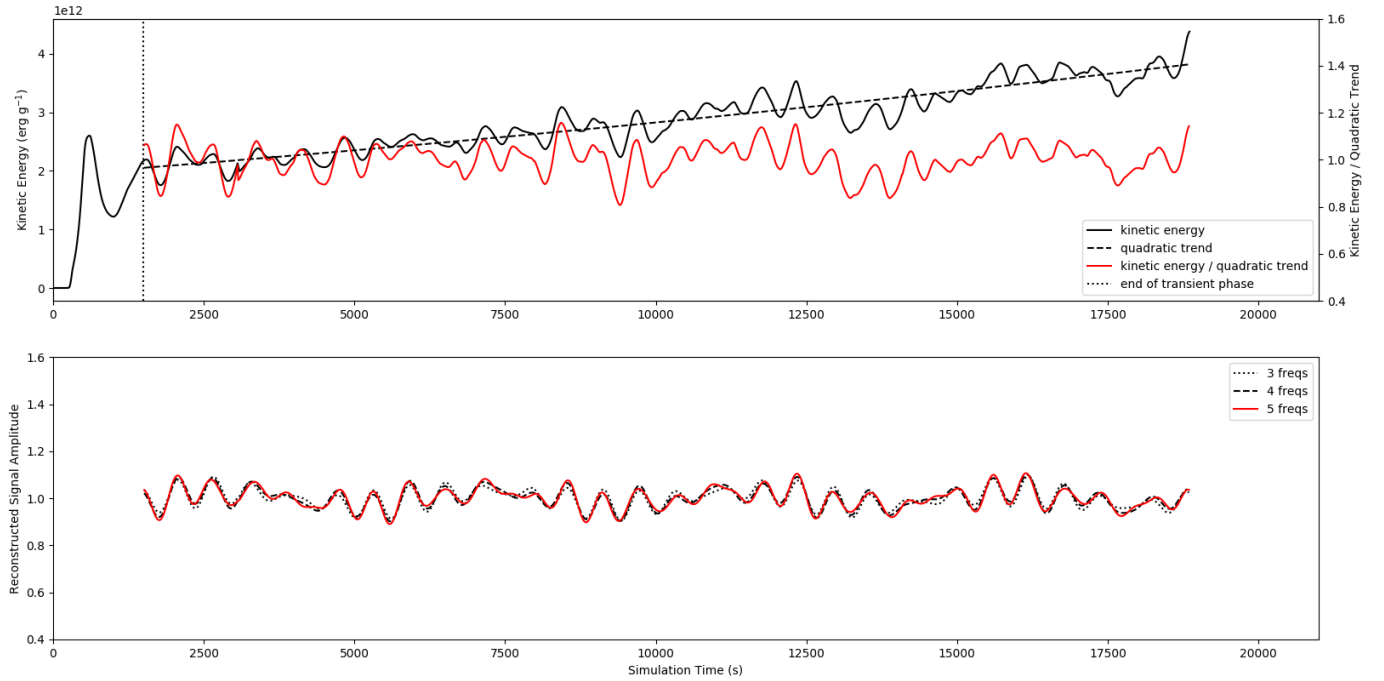


Figure 4. Evolution with PROMPI of the turbulent kinetic energy in a small section of the C+C burning shell (top panel), and low order decomposition into modes of 3, 4, and 5 frequencies (bottom panel), after [Cristini, et al. \(2019\)](#). In the top panel the evolution is split into an initial transient phase, to the left of the vertical dotted line, and a longer evolutionary phase, to the right. Here a secular increase is seen, which is due to consumption of fuel and agrees with the 1D model. If this is allowed for, the result is the red line, which is not static, but has a stable average over 30 pulses. The bottom panel shows the dominant modes corrected for the quadratic trend, as three approximations (3, 4, and 5 frequencies). Finite variability is maintained because the computational domain is sufficiently small ([Meakin & Arnett 2007b](#); [Arnett, Meakin & Young 2009](#)) to resolve patches of turbulence. The curves lie closely together, indicating that the pulses in TKE are dominated by these 3 low order modes, consistent with [Holmes, Lumley & Berkooz \(1996\)](#) and §3.2. The initial transient phase provides a direct estimate of the cascade ratio in the simulations (see §3.4.2; [Onsager 1949](#)). The initially flat pre-rise phase (far left top panel) shows no motion until thermal burning builds a superadiabatic excess to accelerate matter. This is a measure of the “turn-over” time.

If we do not ignore phase lags, we get Fig. 4, which shows the TKE, for a 256^3 ILES from onset through 30 pulses. In this approximation to a section of the whole shell, a quasi-steady state of bounded pulses is formed. By their interaction the pulses suggest the presence of several low order modes. Following (Holmes, Lumley & Berkooz 1996), we find by a Karhunen-Loève decomposition of the time series, that three low order modes are indeed dominant. For this particular case there is also a slow evolution due to increasingly active thermonuclear burning, which agrees well with predictions of 1D evolutionary models. There is no indication of any growing instability on a shorter or similar timescale.

3.5. Other dynamic terms

Our ILES include all terms relevant for turbulence, but this is not true for MLT: it omits some acceleration terms needed for the strong stratification case (which cannot be isotropic, for example). Despite these and other objections, MLT works in some sense (Renzini 1987). Why? Part of the reason was given in Paper I (Arnett, et al 2019); here we examine the issue further.

In a steady state and in a co-moving frame, the work done by fluctuations is balanced by turbulent dissipation (Eq. 11); see also (Meakin & Arnett 2007b; Nordlund, Stein, & Asplund 2009). For weak stratification this can be reduced to the MLT balance between drag and buoyancy alone (§3.3), but there are additional terms in general, which we derive.

Using the identity

$$P'\nabla \cdot \mathbf{u}' + \mathbf{u}' \cdot \nabla P' = \nabla \cdot (\mathbf{u}'P'), \quad (14)$$

we obtain after averaging

$$-\langle \overline{\mathbf{u}' \cdot \nabla P'} \rangle = W_B + W_P + \mathcal{A}. \quad (15)$$

We give the definitions below.

3.5.1. The buoyancy term W_B

In MLT the net mass flow is zero, so inflowing density excesses and deficits are balanced. If the flow is strongly subsonic, the perturbations in temperature, density and composition give small pressure perturbations (e.g., Fig 3). This is the “buoyancy” limiting case, and the work done by buoyancy W_B is

$$W_B = \langle \overline{(\rho' \mathbf{u}' \cdot \mathbf{g}) \beta_T \Delta \nabla} \rangle, \quad (16)$$

which uses the acceleration due to the entropy excess (Eq. 8) in MLT (Viallet, et al. 2013).

We have randomly perturbed a hydrostatic initial model by mass-conserving density variations of low amplitude which, for no change in pressure or composition,

imply entropy variations. Interesting behavior results: stable regions ($\theta > \frac{1}{3}$) quickly damp these small blemishes by sound wave radiation, while unstable regions ($\theta \leq \frac{1}{3}$) begin growing them exponentially, at first attempting to form small convective rolls from the variously distributed torques. Because of the choice of initial conditions, the power of the fluctuations is at the grid scale at first, but nonlinear evolution continues until a global turbulent region develops, powered by burning at the integral scale (Fig. 1).

3.5.2. Pressure dilatation term W_P

The next important term in Eq. 15 is the work done by turbulent pressure fluctuations P' on the turbulent flow, the “pressure dilatation”. For weak stratification **and low Mach number**, $W_P \approx 0$ by up-down symmetry in the mass flux, but for strong stratification,

$$W_P = \langle \overline{P' \nabla \cdot \mathbf{u}'} \rangle \sim \langle \bar{\rho} \rangle \langle \overline{u_r'^3} \rangle / H_\rho, \quad (17)$$

where we use $P' \sim \langle \bar{\rho} \rangle u_r'^2$, and $\nabla \cdot \mathbf{u}' \sim u_r' / H_\rho$ (Viallet, et al. 2013).

When the convective Mach number is small, so is the turbulent pressure fluctuation P' . In this limit the flow has little effect on the background structure, and is nearly anelastic. As the flow becomes more stratified (more plume-like), W_P becomes nonlocal and more important relative to W_B .

3.5.3. Acoustic and turbulent kinetic energy fluxes

The KE equation involves two turbulent fluxes: the TKE flux $f_k = \langle \bar{\rho} \rangle \langle u_r' \cdot \frac{1}{2} (u_r')^2 \rangle$ and the acoustic flux $f_p = \langle \overline{u_r' P'} \rangle$, so

$$\mathcal{A} = -\nabla_{\mathbf{r}} \cdot (\mathbf{f}_p + \mathbf{f}_k). \quad (18)$$

There is some freedom in the formulation of the kinetic energy equation, especially in the expression which splits the sum of the driving terms; see discussions in (Nordlund, Stein, & Asplund 2009) and (Arnett & Meakin 2011). We split the driving into W_P and W_B as these are thermodynamically the most fundamental quantities: W_B measures the reversible exchange between kinetic energy and potential energy, W_P measures the reversible exchange between kinetic energy and internal energy (Viallet, et al. 2013).

The 3D simulations for C, Ne and O burning are more vigorous than for H or He burning (mildly compressible flow; see §5.1.4), so the acoustic flux term is also small but nonzero (see Fig. 2, Paper I). The divergences of the acoustic flux, and of the turbulent kinetic energy flux, are omitted from MLT.

Cristini, et al. (2019) discuss a series of ILES of the C shell in which the driving by nuclear burning is successively scaled from weak to strong. As the driving

increases the new terms (pressure dilatation and divergences of acoustic and kinetic energy) become important. Due to the increase in acceleration, the shell expands, pulse amplitude increases, and mass is ejected from the grid for the most vigorous burning, connecting mass loss to vigorous convection.

4. WEAK STRATIFICATION

Except for surface convection zones (atmospheres), convection in stars is weakly stratified. This includes all convection driven by quasi-static nuclear burning. Cooling by neutrino emission accelerates the stages of C, Ne and O burning so that, unlike photon-cooled stages (H and He), more powerful methods of fluid flow simulation become feasible: we choose our time step with a causality (Courant) condition (Leveque 2002), allowing neutral stability of the fluid. Both shell and core burning have weak stratification.

Guided by Onsager’s conjecture (§2.1.1), we use Eq. 5 to extract “effective” damping lengths ℓ_d from our 3D simulations with no new assumptions. This provides an absolute scaling for the ILES in Fig. 2 and the anomalous damping implied by our ILES.

Despite having no imposed viscosity, our ILES reproduce a statistically steady convection zone for 30 turnover times, as Fig. 4 showed. Our initial models and 3D simulations are already consistent, so $\overline{\langle \epsilon_{nuc} \rangle} = W_B / \langle \bar{\rho} \rangle$.

For weak stratification we follow Viallet, et al. (2013), keep only the buoyancy term (Eq. 16) in Eq. 15, and use Eq. 13 in Eq. 11. We assume acoustic and TKE fluxes are small. If driving equals damping on average,

$$\overline{\langle \epsilon_{nuc} \rangle} = W_B / \langle \bar{\rho} \rangle = -\overline{\langle u_r^3 \rangle} / \Delta_{cz}, \quad (19)$$

where each term may be independently evaluated from the ILES. We define a consistency factor

$$\mathcal{C} \equiv -\overline{\langle u_r^3 \rangle} / \overline{\langle \epsilon_{nuc} \rangle} = \ell_d / \Delta_{cz}, \quad (20)$$

which would be unity if $\ell_d = \Delta_{cz}$, i.e., if the ILES are consistent with Onsager ideal turbulence in weak stratification.

Interior convection seems insensitive to uncertainties related to atmospheric physics, and thus is primarily a turbulence problem. Entrainment remains a key issue (Scott, et al. 2020). High resolution ILES give reasonably consistent results for the short term dissipation rate (Porter & Woodward 2000; Meakin & Arnett 2007b; Arnett, Meakin & Young 2009; Arnett, et al. 2015; Jones, et al., 2017; Cristini, et al. 2017), as do experiment (Vasilicou 2015).

4.1. The O+O shell

Fig. 5 shows the time-averaged rate of anomalous dissipation (§2.1.1) of turbulent kinetic energy, weighted by the increment in spherical mass coordinate, versus radius, $\bar{\epsilon}_K \times 4\pi r^2 \rho$ for the oxygen burning shell at several different numerical resolutions. Here the time average $\bar{\epsilon}_K$ must be supplemented by a space average to obtain $\langle \bar{\epsilon}_K \rangle$ in Eq. 5. The dissipation due to the turbulent cascade is relatively flat; most of the variation in Fig. 5 is in the mass increment factor. Convection automatically chooses its boundaries, which are sharply defined at $\theta = 1/3$ (§2.1.1).

The “slope” feature in Fig. 5 (between $r \sim 0.43$ and 0.85×10^9 cm) has a constant gradient which is not sensitive to zoning in space, from 128^3 to 1536×1024^2 , and has a Kolmogorov-like value over the averaging window in time, which agrees with Eq. 5.

This is a result of our ILES, confirming Arnett, Meakin & Young (2009), and not an imposed assumption. It is (i) a numerical realization of damping (§2.1.1) by emergent nonlinear effects (§3.4), and (ii) a confirmation of our Reynolds stress expression (Eq. 13).

The amplitude of the “slope” shows a mild fluctuation with zoning, despite being averaged over a few turnover times. Dissipation goes to zero abruptly at the lower boundary interface which separates the convective from the non-convective layer. The flow in the upper and lower sandwiching layers is “smooth” ($\theta > \frac{1}{3}$) being wave-like, instead of turbulent (“rough”, $\theta < \frac{1}{3}$); see §2.1.1).

Inadequate resolution at the lower boundary is easily identified as a different “spike” for each choice of zoning; these spikes are small, beginning to disappear as zones are added. The spikes occur at the radius of the thin boundary layer (Fig. 1 in Paper I), and are due to 3D waves which sweep past the radial grid coordinate. This error decreases with finer zoning, and corresponds to an inability to resolve the surface waves in the boundary layer on the grid used. The bottom spike is more prominent because the stratification in pressure (and density) is steepest at the bottom of the convective region.

Dissipation in the upper boundary was converged at the range of resolutions shown. This milder condition for numerical convergence on the upper boundary is to be expected because of the larger scale heights in all of the structural and flow fields there.

Unlike the stable regions at $r < 0.43 \times 10^9$ cm and $r > 0.85 \times 10^9$ cm, the convective region has fluid trajectories which, due to mild shocks, give an average dissipation length of $\ell_d \approx \Delta_{cz}$ (Eq. 13).

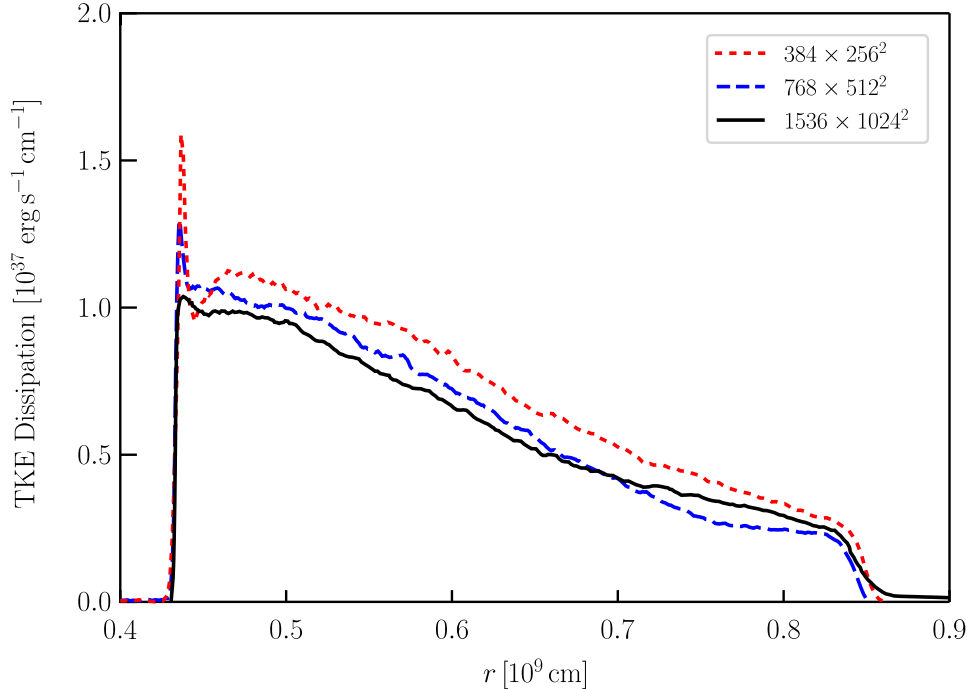


Figure 5. The anomalous dissipation of turbulent kinetic energy $\overline{\epsilon_K}$, plotted as $\overline{\epsilon_K} \times (4\pi r^2 \rho)$ versus radius, for the oxygen burning shell; see §3.4.1. $\overline{\epsilon_K}$ is balanced by generation of kinetic energy by buoyancy, giving a quasi-steady cascade of turbulent kinetic energy as described in §2.4 and §3. The “med-res” (384×256^2 , red dotted line) and “hi-res” cases (768×512^2 , blue dashed line) of (Viallet, et al. 2013), and a “very-hi-res” case (1536×1024^2 , black line) (the “Perth” simulation, see Arnett, et al. 2015) are shown. Using Eq. 2, the Reynolds numbers are $\text{Re}^* \sim 1100, 2800$ and 7000 . The “spike” at $r \sim 0.43 \times 10^9$ cm is due to inadequate spatial resolution of the lower (thinner) boundary layer, and begins to vanish at the highest resolution. The upper boundary layer seems well resolved in space. The remaining dissipation is the “slope” feature between 0.44×10^9 cm $\leq r \leq 0.85 \times 10^9$ cm. It is statistically steady but not static, and is due to dissipation by mild shocks (see Eq. 5; 3.5.2). It is affected by the density gradient, and found to have a Kolmogorov-like intensity on average (Arnett, Meakin & Young 2009). The dissipation is not due to numerical error, but rather to an emergent and robust feature of the nonlinear Euler equations: the turbulent cascade. Onsager’s prediction of $\theta \leq 1/3$ for boundaries is confirmed; see §2.1.1. Ingestion of ^{20}Ne also causes heating and evolution of the background (Mocák, et al. 2018); this is absent in the C+C shell (Fig. 6). The number of turnovers taken to construct the curves is limited by computational cost; med-res, hi-res and very hi-res have 4, 2.1 and $\lesssim 2$ turnovers,

Table 1 summarizes the oxygen-burning shell results in which only the zoning is changed. Here $\alpha_{\text{MLT}} = \ell_d/H_P \approx 2 \approx \Delta_{cz}/H_P$. Structural variables, such as depth of convection zone Δ_{cz} , and density scale height H_ρ , are insensitive to zoning. The rms velocity v_{rms} fluctuates, and the number of turnover times ($t_{\text{ave}}/t_{\text{to}}$) used in time averages are shown. All of our ILES show convection as episodic (Meakin & Arnett 2007b; §3.4.2), with a fluctuating behavior, but steady on average.

The oxygen burning simulation begins with entrainment of ^{20}Ne into the ^{16}O shell, giving two burning zones in the same convective shell (Mocák, et al. 2018)¹⁵. Arnett, et al. (2015) discuss our highest resolution simulation (“Perth”) of the oxygen-burning shell.

ILES numerical simulations for weakly-stratified convection produce a dissipation which agrees with Kolmogorov theory for homogeneous, isotropic turbulence. The estimates of the consistency factor \mathcal{C} are roughly unity for all resolutions:

$$\mathcal{C} = \ell_d/\Delta_{cz} \rightarrow 0.90, 1.16, 1.31, 1.12, \quad (21)$$

despite the Ne ingestion episode, which seems to affect these numerical results slightly ($\pm 15\%$); see also (Mocák, et al. 2018), and below.

4.2. The C+C shell

Figure 6 shows the time-averaged anomalous dissipation over the carbon burning shell as a function of radius, in the same format as Fig. 5; see Cristini, et al. (2017, 2019). Unlike the previous simulations, there is no ingestion of a new and different fuel (^{20}Ne), so the evolution is smoother (see Mocák, et al. 2018 for further discussion

¹⁵ This was also seen in carefully modelled proton ingestions into He-burning convection zones (Mocák et al. 2010; Fujimoto, Ikeda & Iben 2000; Campbell, Lugaro & Karakas 2010).

Table 1. Dissipation lengths: O+O shell, $\Delta_{cz} \sim 2H_P$

stage	zoning depth \times area	Δ_{cz} 10^8cm	ℓ_d 10^8cm	ℓ_d/Δ_{cz} $= \mathcal{C}$	ℓ_d/H_P	v_{rms} 10^7cm s^{-1}	$t_{\text{ave}}/t_{\text{to}}$
O shell ^a	400×100^2	4.0	3.6	0.90	1.48	0.97	4
O shell ^b	192×128^2	4.2	4.9	1.16	2.03	1.07	4
O shell ^b	384×256^2	4.2	5.5	1.31	2.27	1.09	4
O shell ^b	786×512^2	4.2	4.7	1.12	1.94	1.09	2.1
O shell ^c	1536×1024^2	4.2	$\lesssim 2$

^aMeakin & Arnett (2007b); oxygen burning with ^{20}Ne entrainment.

^bViallet, et al. (2013); oxygen burning with ^{20}Ne entrainment.

^cArnett, et al. (2015); oxygen burning with ^{20}Ne entrainment (“Perth”).

of ^{20}Ne ingestion). The very weak energy generation is boosted by 10^3 (to be merely weak). This gave a shorter burning time (still many turnovers), no noticeable structural change, but more computational efficiency in this C+C simulation; see Cristini, et al. (2017). The higher “spike” errors, seen in C+C relative to O+O, are due to our choice of pseudo-cartesian coordinates here, which were computationally faster but less accurate than the true spherical ones used for O+O.

These results are consistent with the oxygen shell simulations, but simpler due to the lack of a ^{20}Ne ingestion episode. Again, the boundary dissipation spike (Cristini, et al. 2017, Fig. 10) tends to disappear at the highest resolutions, while the “slope” (anomalous dissipation) is insensitive to zoning (Cristini, et al. 2017, Fig. 9).

Table 2 shows the results of ILES for C+C shell burning. There are (4.0, 4.4, 10.6, 1.5) turnovers for zoning of (128^3 , 256^3 , 512^3 , 1024^3), so the highest resolution in space corresponds to the poorest statistics in time because of budgetary limitations and the need to disentangle the behavior caused by intermittency. The cases with highest spatial resolution have fewer turnovers, and lose some statistical accuracy. We have

$$\mathcal{C} = \ell_d/\Delta_{cz} \rightarrow 1.05, 1.01, 1.005, 1.08, \quad (22)$$

so the dissipation length is close to the depth of the convection zone.

As with O+O, runs of greater duration at higher resolution are desired, but there already seems to be a clustering around $\ell_d/\Delta_{cz} \approx 1.0$. The C+C shell is slightly more stratified than the O+O shell, with a depth of 3 rather than 2 H_P . Deeply stratified convection zones have smaller values of ℓ_d/Δ_{cz} (see §5), so this C+C result seems consistent with the previous O+O one.

4.2.1. Resolution issues

Figures 5 & 6 provide insight into the zoning required to spatially resolve the thin lower boundary layer. The “Perth” simulation of the O+O shell, at 1536×1024^2 , already seems to be reducing the “spike” into a merger with the “slope”, although we have few turnovers for such a short duration in time (see Table 1). Errors in the dissipation rate due to coarse zoning (the “spikes” in Figs. 5 & 6) appear to be converging toward zero with higher resolution, while the “slope” (anomalous dissipation due to the cascade in the $\theta \leq 1/3$ region) is robustly nonzero.

The composition profiles also converge to a fixed shape (Cristini, et al. 2019, their Fig. 16). This is due to dissipation, but a *dissipation which is constrained by the turbulent cascade* (Fig. 2). A turbulent boundary layer develops between convective and non-convective regions, which ILES seems to represent robustly.

A related problem is that of the resolution of entrainment (Meakin & Arnett 2007b; Cristini, et al. 2017; Scott, et al. 2020), which may involve the turbulent boundary layer. Woodward et al. (2015) have shown that the entrainment rate in a simulation depends upon the zoning, and with due caution, suggest that their 1536^3 may already capture the Kelvin-Helmholtz waves (which they and we believe drive the entrainment). This seems consistent with our “Perth” simulation, which does not have the factor of 3 zoning advantage of piecewise-parabolic boltzmann advection of Woodward et al. (2015), but does have the improved brute-force resolution of a “box-in-star” grid (Arnett, et al. 2015), which allows local enhancement of zoning in the box relative to the whole star.

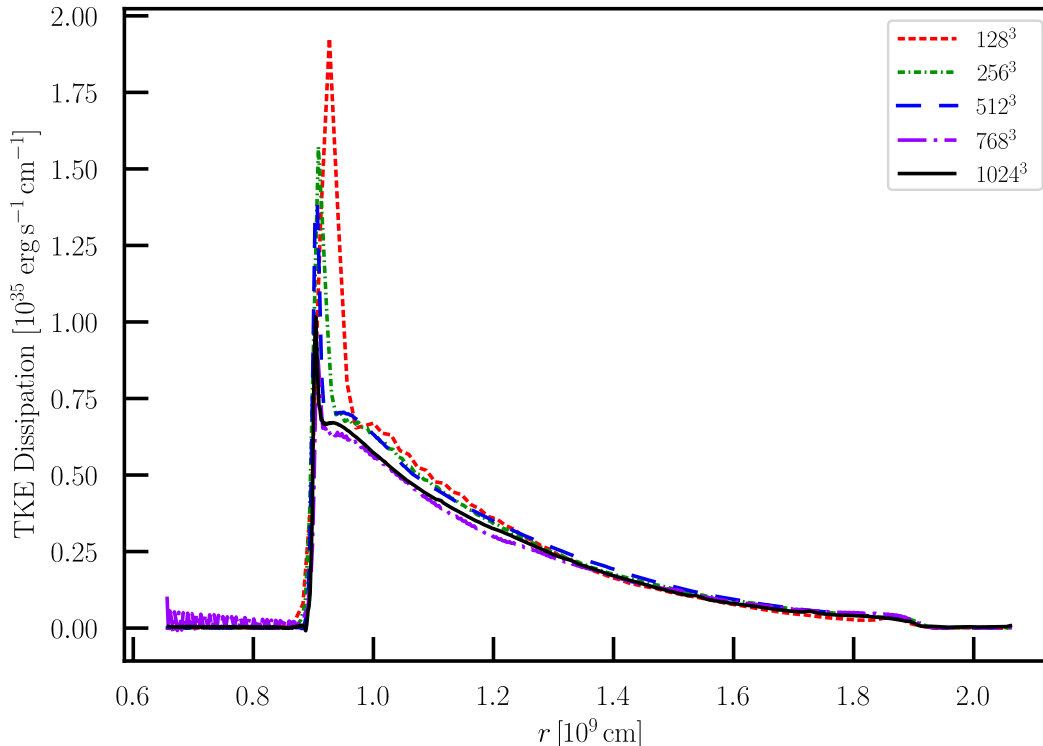


Figure 6. The anomalous dissipation of turbulent kinetic energy $\overline{\epsilon_K}$, plotted as $\overline{\epsilon_K} \times 4\pi r^2 \rho$ versus radius, for the carbon burning shell. $\overline{\epsilon_K}$ is balanced by generation of kinetic energy by buoyancy, giving a quasi-steady cascade of turbulent kinetic energy (§3). Simulations of 128^3 , 256^3 , 512^3 , 768^3 , and 1024^3 (Cristini, et al. 2017, 2019) are shown. Using Eq. 2, the Reynolds numbers range from $Re \sim 256$ to 4096. Strong intermittency is associated with the pulses in turbulent kinetic energy (Fig. 2 of Arnett, et al 2019), and requires time averaging (see text). Unlike the O+O simulation, the simpler burning associated with C+C has no strong ingestion of new fuel, requiring readjustment of the structure, but the effect of finer zoning seems similar. The sharp “spike” is due to numerical error, and monotonically decreases in size with increased resolution. However the broad “slope” in the dissipation profile is an emergent and robust feature of the nonlinear Euler equations (the turbulent cascade), and converges with resolution toward an asymptotic form $\overline{\epsilon_K}$ for damping (see Eq. 5; 3.5.2). Onsager’s prediction of $\theta \leq 1/3$ for boundaries is confirmed; see §2.1.1.

4.2.2. Dynamic constraint and dissipation anomaly

The Onsager conjecture (§2.1.1) implies that the high frequency fluctuations (turbulence) will cause the spatial part of the advection operator to act as damping *on average* (§3.4.1). This is equivalent to $\ell_d \approx \Delta_{cz}$ in Table 2. Even with no explicit dissipation term ($\nu_{NS} \equiv 0$), our ILES generates a spontaneous turbulent damping which is equivalent to Eq. 13; see also De Lellis & Sze’kelyhidi (2013); Eyink & Drivas (2018a). This adjusts to balance turbulent driving, on average, in a steady state.

The dissipation is not an adjustable parameter, but due to shocks in the nearly inviscid flow. This gives an added statistical constraint on the self-consistency of the flow: on average the damping and driving must balance.

It also implies a constraint for the velocity spectra in Fig. 2, which fit the Kaneda, et al (2003) curve.

It is striking that by purely numerical experiments with the Euler equations, without using any viscous term, we recover Eq. 3, which is the Kolmogorov result for dissipation in a turbulent cascade.

As we refine our zoning the global dissipation rate converges quickly, as Onsager (1949) anticipated; for 256^3 zoning and higher, the total dissipation rate changes little. There is no kinematic viscosity ν_{NS} . The effective value of the Reynolds number (§2) must be sufficiently large (Onsager 1949; Eyink & Sreenivasan 2006), so that shocks provide the dissipation in the inviscid limit, which they do.

5. STRONGLY-STRATIFIED CONVECTION

Table 2. Dissipation lengths: C+C shell^a, $\Delta_{cz} \sim 3.0H_P$

stage	zoning depth ³	H_P 10 ⁸ cm	Δ_{cz} 10 ⁹ cm	ℓ_d 10 ⁹ cm	ℓ_d/Δ_{cz} = \mathcal{C}	ℓ_d/H_P	v_{rms} 10 ⁶ cm s ⁻¹	t_{ave}/t_{to}
C shell	128 ³	3.22	1.030	1.08	1.05	3.35	3.76	3.99
C shell	256 ³	3.47	1.033	1.04	1.01	3.00	4.36	4.37
C shell	512 ³	3.41	1.025	1.03	1.005	3.02	4.34	10.6
C shell	1024 ³	3.43	1.009	1.09	1.08	2.94	3.93	2

^aCristini, et al. (2017); boosted carbon burning, pseudo-cartesian grid.

The most strongly stratified convection occurs near stellar surfaces (atmospheres). This brings additional complications, some of which may not be negligible.

The base of a convective shell has higher sound speed and smaller scale height, so the Courant condition on the time step is more restrictive. These effects cause fluid dynamic simulations to become more challenging. While our previous ILES are well suited for multi-processing, scaling well on multiple cpus as well as graphics cards at a convective Mach number ≥ 0.005 , this is not yet true for lower Mach number flow.

Do the neglected acceleration terms (§3.5) become important with strong stratification? Strong stratification breaks the up-down symmetry (assumed in MLT), so that a strong negative flux of TKE occurs, giving a strong nonlocal, radial coupling in the flow.

In a co-moving frame, fast, dense, narrow downflows (which move into higher pressure) must be balanced by slow, less-dense, wide upflows (which move into lower pressure), as was the case for weak stratification. However, as the up-down asymmetry grows, acceleration by “pressure dilatation” can not be ignored, giving negative fluxes of TKE. LES of strongly stratified atmospheres (Stein & Nordlund 1989; Nordlund, Stein, & Asplund 2009; Asplund, Ludwig, Nordlund & Stein 2000) showed such negative TKE fluxes. Meakin & Arnett (2010) showed that this was a feature of strong stratification, not of top versus bottom driving. *MLT ignores the fluxes of turbulent kinetic energy, not because they are small relative to enthalpy fluctuations (they are not; see Eq. 7), but because they are assumed to cancel by up-down symmetry* (Böhm-Vitense 1958, 1989).

5.1. RG simulations

We base our discussion of strongly-stratified convection on the “red giant” (RG) simulations of Viallet, et al. (2013), which were done with the MUSIC code (Viallet, et al. 2011). The Euler equations were solved with implicit time stepping. MUSIC allows larger time steps in the deep, most nearly static regions, but at the ex-

pense of higher computational cost per step. MUSIC allows small flow speeds but does not ignore sound waves (i.e., no anelastic approximation). Time steps were chosen based on a causality (Courant) constraint on *fluid flow*, instead of *sound speed* as in PROMPI. Despite the completely different solvers, these simulations agree well with ILES from PROMPI where they overlap.

Simulations of convection in stellar atmospheres (Asplund, Ludwig, Nordlund & Stein 2000) focus on the outer layers where the observed photon spectra are formed. Viallet, et al. (2011, 2013) focused instead on the deep layers¹⁶ of the surface convection zone.

5.1.1. The initial state

The stellar structure code used to construct the initial model is described in Baraffe & El Eid (1991). MLT was used (with $\alpha = 1.7$) to treat convection, and the extent of the convective region was based on the Schwarzschild criterion. The structure was integrated from the photosphere down to 20% of the stellar radius, avoiding the nuclear burning region. This initial stratification¹⁷ became a starting model for the 3D hydrodynamic code.

Convection extended down to $r \sim 2.3 \times 10^{12}$ cm, nearly half of the stellar radius. The nuclear burning region was not included in the computational domain, instead a radiative flux corresponding to the stellar luminosity was imposed at the inner boundary. The surface layers were characterized by strong superadiabatic stratification, which would be explicitly resolved in stellar atmospheres simulations; as in Viallet, et al. (2011), a proxy was used.

The RG simulations explicitly calculated a dynamic lower boundary for turbulent convection. A boundary layer was formed, similar in character to that at

¹⁶ This might be where a tachocline would develop.

¹⁷ Such a model would correspond to a $5M_{\odot}$ star at the end of central He burning, finishing its blue loop and evolving toward lower T_{eff} and away from the red edge of the Cepheid instability strip (Baraffe & El Eid 1991).

the lower arrow in Fig. 1. Despite coarser zoning, the RG lower boundary resembles that in Fig. 4, Arnett, et al. 2015, which shows vertical and horizontal velocities, composition gradient, and wave emission into the convectively stable region. Below this is a non-convective radiative region.

The steep gradient approaching the atmosphere was replaced by an approximate boundary condition (Newtonian cooling), giving a depth of 7.8 pressure scale heights of turbulence on the grid¹⁸. The initial 1D model had a stratification of 14.3 pressure scale heights, with the additional 4.5 pressure scale heights absorbed into the Newtonian cooling region, reducing the total stratification which was active dynamically.

These choices may be considered to complement those used for 3D simulation of stellar atmospheres, emphasizing physical effects which are characteristic of the deeper layers, rather than the atmosphere, while avoiding artificial dissipation.

5.1.2. Flaws in Atmosphere and RG simulations

There are weaknesses in both the RG simulations (at the upper boundary), and the LES of atmospheres (at the lower boundary). In order to “stabilize the numerical algorithms” (Stein & Nordlund 1989; Stein, Nordlund & Kuhn 1989b), adjustment of the dissipation in stellar atmospheres seems¹⁹ to result in more laminar flow at the bottom of the computational volume, even though the plasma there should be highly turbulent. Such a numerical effect could distort fast downflows. In §2.3.2 and Fig. 2, hyperviscosity codes were shown to have a defect (the “bottleneck”) in the velocity spectra relative to ILES and higher resolution DNS. This flaw seems to have little effect on the predicted stellar spectra (Nordlund, Stein, & Asplund 2009; Magic, et al. 2013), but may affect the deep flows (Hanasoge, Gizon & Sreenivasan 2016).

In the RG simulations, the Newtonian cooling approximation has a similar effect of smearing fast downflows. These ILES should have a deficit, relative to reality, of narrow fast downflows at the top of the convective region, which in stellar atmospheres would already appear in the 4.5 scale heights absorbed in the Newtonian cool-

ing boundary, and which may propagate to the lower boundary as even narrower downflows for high Re. The two types of simulation may be wrong in the same sense.

The integral Re for the solar convection region, $Re \sim 10^{14}$, is far higher than our attainable computational one, $Re^* \lesssim 1.7 \times 10^4$ (see §2, and Hanasoge, Gizon & Sreenivasan 2016; Arnett & Meakin 2016). Our estimated Re for the anelastic ASH code (Miesch, et al. 2009), and for the hyperviscosity STAGGER code (Nordlund, Stein, & Asplund 2009), is far lower than for the 1024³ (Cristini, et al. 2017) and 1536³ (Woodward et al. 2015) ILES.

5.1.3. Numerical Results

With these issues in mind, we now examine strongly stratified convection from the MUSIC simulations.

TKE fluctuates strongly; compare Arnett, et al 2019 (Fig. 2) and Viallet, et al. 2013 (Fig. 2). The lower boundary quickly relaxes to a turbulent boundary layer²⁰, as seen in the weak stratification simulations (see also Arnett & Moravveji 2017).

Table 3 summarizes the RG simulations, to be compared with those in §4 for weak stratification. The lower resolutions shown, relative to Table 1 & 2, reflect the greater computational load²¹ of the implicit hydrodynamic solver in the MUSIC code (see discussion in Meakin & Arnett 2007b; Viallet, et al. 2013; Woodward et al. 2015). We estimate an effective Reynolds number Re^* as in §2.2.

Differences caused by stratification are: (i) the TKE flux is nonzero, (ii) acceleration by pressure dilatation is nonzero, (iii) waveforms change from rolls to plumes²², and (iv) the dissipation length ℓ_d (§3) decreases to less than the depth of convection Δ_{cz} . Strong stratification implies a more spherical geometry, so that large wavelength global modes may be important (e.g. Woodward et al. 2015; Jones, et al., 2017). Highly stratified convection with a localized source of turbulence will have a significant flux of turbulent kinetic energy, and thus is nonlocal, unlike MLT. The radial flux of turbulent kinetic energy is negative and a significant fraction in magnitude ($\sim 35\%$) of the enthalpy flux. Convection is

¹⁸ For the solar convection zone, a depth $\Delta_{cz} \gtrsim 20H_P$ would be better, but $7.8H_P$ is sufficient to show some of the qualitative modifications due to stratification.

¹⁹ This appears from a visual comparison to demonstrably turbulent flows (e.g., Meakin & Arnett 2007b). It might also be expected from a “bottleneck” spectrum; §2.4. An authors’ estimate of the Re in the bottom layers of the atmospheric LES, would be helpful. From Eq. 2 we estimate $Re^* < 90$ for Trampedach & Stein (2011), a factor of 4 higher (360) for Magic, et al. (2013), but smaller for “stabilized” flows.

²⁰ The thermal relaxation time for integral scale radiative diffusion is much longer for laminar flow than for turbulence, due to the turbulent cascade to smaller scales.

²¹ MUSIC would be superior to PROMPI at the lowest Mach numbers, but neutrino cooling speeds the evolution for C, Ne and O burning, avoiding these lower velocities.

²² Compare these 3D simulations (Viallet, et al. 2013) to 2D MUSIC simulations of Pratt, et al. (2017).

Table 3. Dissipation lengths: Red Giant, $\Delta_{cz} \sim 7.8H_P$ on grid

stage	zoning depth \times area	Δ_{cz} (cm)	ℓ_d (cm)	ℓ_d/Δ_{cz}	v_{rms} (cm/s)	t_{ave}/t_{to}	Re^*
RG ^a	216×128^2	2.0×10^{12}	7.0×10^{11}	0.350	2.27×10^5	3.3	256
RG ^a	432×256^2	2.0×10^{12}	7.7×10^{11}	0.385	2.34×10^5	3.3	645

^aViallet, et al. (2013); red giant, only bottom of convection zone (see text).

driven to a significant extent ($\sim 40\%$) by “pressure dilatation”, W_P , in addition to buoyancy.

Viallet, et al. (2013) show that W_P is negligible if $H_\rho \gg \ell_d$ and becomes comparable to the dissipation rate for $H_\rho \ll \ell_d$. The ratio of turbulent ram pressure to local pressure, $\rho u'^2/P$, ranges from $\sim 2 \times 10^{-3}$ at the bottom, to $\sim 2 \times 10^{-2}$ at the top of the convection zone (Viallet, et al. 2013, Fig. 3 and §4.1.1). In coordinates co-moving with the matter, the quadratic dependence on u' of turbulent pressure fluctuations act on the flow to give a *net acceleration downward*. *The cubic dependence on u' causes the fastest motion to dominate the TKE, so the tendency of buoyancy to produce negative TKE flux is strengthened.*

Because of the large heat content, the total energy flux is still positive. The ratio of kinetic energy flux to enthalpy flux²³ is $\sim (1/\Gamma - 1) = -0.4$ for $\Gamma = 5/3$, which is approximately the same as the averaged numerical result for the deep interior of the red giant (-0.35).

The luminosity has a more complex dependence on adiabatic excess $\Delta\nabla$ than in MLT: it includes the luminosity due to turbulent kinetic energy L_{TKE} , which is negative, and may affect the inferred stellar luminosity. In standard stellar evolution, this error must be absorbed (if possible) into the calibration of the mixing length.

5.1.4. Asymptote for strong stratification

Our ILES have all the relevant acceleration terms (although modest resolution); we now explore approximations which capture the physics. The turbulent kinetic equation for a quasi-steady state is,

$$-\langle \mathbf{u}' \cdot \nabla P' \rangle = W_B + W_P - \rho \epsilon_K - \nabla_{\mathbf{r}} \cdot (\mathbf{f}_k + \mathbf{f}_p). \quad (23)$$

A transition region from weak to strong stratification occurs as $\Delta_{cz} \gtrsim H_\rho$. Each limit tends to be associated

*with a flow morphology. If $\Delta_{cz} \lesssim H_\rho$, W_P is small, and we recover the weak stratification result (convective rolls, §4). In the strong stratification case, W_P adds to the driving of *convective plumes* (Viallet, et al. 2013).*

Averaging over several turnovers is required for a sufficiently smooth curve to be an extension for the time independent cubic equation of Böhm-Vitense (1958). W_P , W_B and ϵ_K track each other, in a cycle of potential energy, kinetic energy, and internal energy maxima (Viallet, et al. 2013, §5).

The simplest case is a steady state with no convective zone growth, thin boundary layers, and small wave flux (Viallet, et al. 2013, Eq. 32, Fig. 7), so

$$W_B + W_P \approx \langle \bar{\rho} \rangle \epsilon_K. \quad (24)$$

The buoyancy work is

$$W_B = \overline{\langle (\rho' \mathbf{u}' \cdot \mathbf{g}) \beta_T \Delta \nabla \rangle} \approx \langle \bar{\rho} \rangle \langle v \mathcal{B} \rangle \quad (25)$$

Since each term in Eq. 24 has been averaged in space-time, this defines an envelope of values for a quasi-steady state.

For strong stratification²⁴, $\Delta_{cz} \gg H_\rho$, and using Eq. 17, we have

$$W_P = \langle \overline{P' \nabla \cdot \mathbf{u}'} \rangle \sim -\langle \bar{\rho} \rangle \langle \overline{u_r'^3} \rangle / H_\rho, \quad (26)$$

so that a generalization of the MLT cubic equation is

$$\langle \overline{v \mathcal{B}} \rangle \approx \langle \overline{u_r'^3} \rangle / \Delta_{cz} + \langle \overline{u_r'^3} \rangle / H_\rho \quad (27)$$

where both buoyancy and pressure dilatation affect the acceleration of flow, but with opposite signs. Turbulence resists being compressed into a smaller volume.²⁵ The $v \mathcal{B}$ term is important for buoyancy braking at boundaries (Arnett, et al. 2015; Arnett, et al 2019).

If $\Delta_{cz} \gg H_\rho$, this gives the effective damping length ℓ_d in the strong stratification limit (convective plumes), so we obtain a strikingly simple limiting case,

$$\alpha \equiv \ell_d / H_P \approx H_\rho / H_P = \Gamma_1, \quad (28)$$

²³ Consider an idealized case: a parcel of gas is dropped, changing potential energy PE into kinetic energy KE. This is then thermalized, and slowly raised to its initial height. The ratio of kinetic energy to enthalpy is $1/(\Gamma - 1)$.

²⁴ See discussion of “pressure-dilatation defect” in (Eyink & Drivas 2018a).

²⁵ This may be important for core collapse supernovae.

where Γ_1 is the adiabatic index of Chandrasekhar (1939):

$$\Gamma_1 = \beta + \frac{(4 - 3\beta)(\gamma - 1)}{\beta + 12(\gamma - 1)(1 - \beta)}, \quad (29)$$

and where $\gamma = c_P/c_V$ is the ratio of specific heats and β is the ratio of gas pressure to total pressure. The appearance of Γ_1 is due to the historical choice of using the pressure scale height H_P for measuring mixing length.

Even the averaged value of Eq. 28 can be complex in regions of partial ionization and dissociation, so a detailed atmosphere may be required for precision (but see §6; Magic, Weiss, & Asplund 2015).

5.1.5. Length scales in strong stratification

It is challenging to resolve a lower boundary for both strong stratification and vigorous turbulence. The numerical data trend toward the asymptotic limit we have derived, even though our largest stratification on the grid is only $\Delta_{cz}/H_P \sim 7.8$, much less than the Sun ($\Delta_{cz}/H_P > 20$).

For strong stratification, the “effective mixing length” asymptotically approaches the density scale height, due to the action of the pressure dilatation term (not in MLT). This confirms a “saturation” behavior noticed by Arnett, Meakin & Young (2009) based upon cruder simulation data. For strong stratification and complete ionization, the “mixing length” ($\ell_d/H_P \sim 5/3$) really does resemble a universal constant (see §6), a behavior unexplained in MLT (Renzini 1987).

6. HRD ESTIMATES OF α_{MLT}

As we saw in §3.3, specifying a mixing length in MLT is equivalent to specifying a global damping length for turbulence, to the extent possible in an incomplete theory like MLT. In §4 and §5 we evaluated damping lengths *self-consistently with the predicted flow, and accounted for anomalous dissipation (Onsager 1949)*, for both weak and strong stratification, without using any parameterized viscosity. We now compare our estimates to published values of “the stellar mixing length parameter” from a representative variety of methods.

6.1. Stellar Evolution alone

Table 4 shows several published values of the constant $\alpha_{\text{MLT}} = \ell_{\text{MLT}}/H_P$ from MLT calculations of stellar evolution; these have been successfully used to fit the observed HR diagram (HRD). For the main sequence to the giant branch, the stellar evolution values are essentially tests of the deep properties of surface convection zones of stars of mass $M \gtrsim 1M_\odot$; apparently they have strong stratification and $\alpha_{\text{MLT}} \approx \Gamma_1 \sim 5/3$, as expected from §5.1.4. Why should a single preferred value

of α_{MLT} work for “essentially all stellar evolution sequences” (Renzini 1987)? The weak stratification would not give a such agreement because of changes in the depth of convection zones with stellar mass and evolution, but strong stratification does.

The stellar evolution sequences are in reasonable agreement despite the fact that these values of $\alpha_{\text{MLT}} = \ell_d/H_P \sim \overline{\langle \Gamma_1 \rangle}$ conflate several distinct issues. They represent space-time averages over the convective region rather than local values. For example, Γ_1 may vary significantly through a region of partial ionization, but such effects tend to be diluted by averaging. The effects of ignoring (i) levitation, due to convective pressure fluctuations (Ludwig & Kucinkas 2012), (ii) the flux of turbulent kinetic energy f_k , and turbulent heating in the background energy equation (Porter & Woodward 2000; Viallet, et al. 2013), and (iii) entrainment due to turbulence at the boundaries (Meakin & Arnett 2007b), all make the stellar models incomplete. These errors are lumped together, as are errors in composition (Asplund, et al. 2009), whenever the free parameter α_{MLT} is adjusted.

For most stars, such averages give $\beta \sim 1$ and $\alpha = \ell_d/H_P \rightarrow \Gamma_1 \sim \gamma \sim 5/3$. The difference $\delta_\epsilon \equiv \alpha_{\text{MLT}} - 5/3$ is a measure of consistency between the stellar models and pure 3D simulations of deep turbulent convection, ignoring recombination (atmospheres) and pairs (very late stages). The variation in $|\delta_\epsilon|$ in Table 4 is primarily an indicator of envelope/atmospheric effects, so $\alpha_{\text{MLT}} \sim 5/3$ is a surprisingly good approximation.

Renzini (1987) noted that “...one single value of the free parameter gives a very good fit to stellar radii from the main sequence to the tip of the giant branch...”, so that “MLT is not that bad”.

For extremely massive stars, which are rare, $\Gamma_1 \rightarrow 4/3$. In regions of partial ionization Γ_1 may drop as low as 1.1 (Young, et al. 2001) in the envelopes, as it also does in regions of O+O burning (Table 5 in Arnett, Meakin & Young 2009) due to electron-positron pair formation. However, global hydrostatic equilibrium requires that the average over the whole star satisfies $\langle \Gamma_1 \rangle \geq 4/3$ (Arnett 1996), giving a lower bound for a quasi-static object.

The arguments above suggest (i) why this is so (MLT mimics the universality of the turbulent cascade in a stratified medium), (ii) what the value of that single parameter should be (it asymptotically approaches $\alpha_{\text{MLT}} \sim \Gamma_1 \sim 5/3$ for strong stratification and complete ionization), and (iii) some possible causes of deviations

Table 4. Evolutionary estimates of $\alpha_{\text{MLT}} = \ell_{\text{MLT}}/H_P$

reference to code calibration	α_{MLT}^a	$(\delta_\epsilon)^b$
This paper, strong stratification	$\Gamma_1 \sim 5/3 \sim 1.67$	~ 0
Some stellar evolution sequences:		
Ekström, et al. (2012)	$1.6467 (M \leq 1.25M_\odot)$	~ -0.02
Ekström, et al. (2012)	$1.65 (M > 1.25M_\odot)$	~ -0.02
Bressan, et al. (2012)	1.74	$\sim +0.07$
Maeder (1999)	1.6	~ -0.07
Baraffe & El Eid (1991)	1.7	$\sim +0.03$
Young, et al. (2001)	1.6	~ -0.07

^aWarning: these values conflate several aspects of convection; see text.

^bHere $\delta_\epsilon = \alpha_{\text{MLT}} - 5/3$ which is a measure of the consistency of the stellar models with 3D ILES simulations of ionized, stratified turbulent convection.

(e.g., different atmospheres produce variations of 20 percent or so; Table 5).

Stellar evolutionary sequences use the simplest approach to atmospheres, with a mixing length which is constant in time and space to define the background structure, separating the structure calculation from that of a simplified photon spectrum at the surface.

6.2. Stellar atmospheres

In §2 through §4, a self-consistent treatment of convective physics in deep interiors of stars was developed, having a turbulent energy cascade whose flux was determined by anomalous dissipation (Onsager 1949). No parameterized viscosity was needed. Our ILES represent the highest Re possible with the zoning used. They tend toward Onsager’s “ideal turbulence”, the inviscid limit which is the appropriate generalization of “universal turbulence” (Batchelor 1960) for stellar scales. In §5 acceleration by pressure dilatation was added to describe turbulent convection in strong stratification (plumes), and an asymptotic limit was found, suggesting $\alpha = \ell_d/H_P = \Gamma_1 \sim 5/3$, for the case of complete ionization.

Surface convection requires additional physics for radiation flow in an atmospheric layer, which limits the Re attainable because of the added computational load. Attempts to infer “effective” MLT mixing-lengths from 3D LES of convective stellar atmospheres (Stein & Nordlund 1989; Nordlund, Stein, & Asplund 2009; Magic, Weiss, & Asplund 2015, 2016; Ludwig, Freytag, & Stef-

fen 1999; Muthsam, Kupka & Löw-Baselli, et al. 2010) have focused on photospheric physics rather than fluid flow and turbulence. In practice this has required sacrifice: crude treatment of shocks, low Re, and an inability to accurately describe the anomalous dissipation (§2, 3).

Fortunately the observed photon spectra can be reproduced to high accuracy using a coarse velocity field, one that barely resolves an intergranular lane (e.g., Dravins & Nordlund 1990). While photon spectra may require exceptional effort to replicate, observations only require coarse structure in the velocity field, such as can be provided by a low Re representation of the flow. Despite their complexity, the photon spectra can only weakly constrain the deep flow; asteroseismology is necessary.

Table 5 shows several representative published values of $\alpha_{\text{MLT}} = \ell_{\text{MLT}}/H_P$ recommended from low Re simulations of stellar atmospheres. Magic, Weiss, & Asplund (2015) have carefully reviewed the work cited; see also Magic, et al. (2013); Magic, Collet, Hayek, & Asplund (2013); Magic, Weiss, & Asplund (2015, 2016); Magic & Weiss (2016). Using significantly higher resolution LES with the STAGGER code, they find basic agreement with Trampedach & Stein (2011), for calibrations with the adiabatic entropy value, and deviations up to $\pm 20\%$ from the solar value.

If our arguments and the 3D atmospheres are both correct, we should have agreement in the complete ionization limit ($\langle \Gamma_1 \rangle \sim 1.67$), and should show more discrepancy at low temperatures and pressures, which they do.

The survey of Magic, Weiss, & Asplund (2015), their Fig. 2, spans a typical range of variation. The low gravity-high $\log T_{\text{eff}}$ edge of their Kiel diagram, for MLT

Table 5. Atmospheric estimates (at low Re) of $\alpha_{\text{MLT}} = \ell_{\text{MLT}}/H_P$

reference to code calibration	α_{MLT}^a	$(\delta_\epsilon)^b$
This paper, strong stratification	$\Gamma_1 \sim 5/3 \sim 1.67$	~ 0
Some stellar atmospheres ^c :		
Ludwig, Freytag, & Steffen (1999)(s_{ad} , 2D) ^d	1.3 to 1.75	-0.37 to +0.08
Trampedach & Stein (2011) ^e	1.67 to 2.20	0.0 to +0.53
Trampedach & Stein (2011) ^e (Sun)	1.76	+0.09
Magic, Weiss, & Asplund (2015) (s_{ad})	1.7 to 2.3	0.0 to +0.7
Magic, Weiss, & Asplund (2015) (Δs)	1.8 to 2.4	0.1 to +0.8
Magic, Weiss, & Asplund (2015) (Sun)	1.98	0.31
Some Combinations ^f		
GARSTEC-Eddington	1.70	+0.03
MESA-Eddington	1.67	+0.00
GARSTEC-3DAtmosphere	1.81	+0.14
MESA-3DAtmosphere	1.83	+0.16

^aWarning: these values conflate several aspects of convection and stellar structure.

^bHere $\delta_\epsilon = \alpha_{\text{MLT}} - 5/3$ is a rough measure of the consistency of the models with 3D ILES simulations of ionized, stratified turbulent convection; see text.

^cTo aid the reader, we use published material in an attempt to place very different and complex computations on a consistent scale. See Trampedach & Stein (2011); Magic, Weiss, & Asplund (2015). Experts are invited to suggest improvements.

^dLudwig, Freytag, & Steffen (1999) use the CO5BOLD code.

^eTrampedach & Stein (2011) use “mass-mixing length” as ℓ/H_P ; see also Magic, Weiss, & Asplund (2016).

^fMosumgaard, et al. (2018) compare a classical method (Eddington outer boundary) to fitting with 3D atmospheres.

parameter calibrated with the entropy of the convection zone, is consistent with our estimate of $\alpha_{\text{MLT}} \sim 1.67$. This boundary is roughly paralld by contours of α_{MLT} , down to minimum temperature and maximum gravity, for both solar metallicity, $[\text{Fe}/\text{H}] = 0$, and -2.0. The reason for such behavior is the recombination of H ions, which gives large variation of opacity and Γ_1 through the surface layers. Here $\langle \overline{\Gamma_1} \rangle$ is not a local quantity, but a space-time average, and the general features of the Kiel diagrams of Trampedach & Stein (2011); Magic, Weiss, & Asplund (2015, 2016) can be so understood.

Experience from stellar evolution has shown that α appears to require an increase for giants (> 2.0), which is also indicated in Table 5. The Sun represents a step in this trend; for $M \gtrsim 1M_\odot$ stars spend the main sequence and the ascent of the giant branch in the $1.67 \lesssim \alpha \lesssim 1.8$ region; such values are common in stellar evolution lore (§6.1).

The last four entries in Table 5 compare results from the MESA and the GARSTEC stellar evolution codes, with (i) a simple Eddington atmosphere, and (ii) a full 3D fluid-dynamic atmosphere (Mosumgaard, et al. 2018). The combined differences in codes and atmo-

spheres is less than 10%. It appears that the inferred value of α_{MLT} is surprisingly insensitive to turbulence, and even to the widely varying details of atmospheric physics (Trampedach, et al. 2014). The simplest boundary condition (Eddington) gives close to our estimate for full ionization, only shifting by 10% from the average with use of 3D atmospheres.

6.3. The Depth Problem for Velocity

The geometric confusion inherent in 1D models faded with the introduction of 3D fluid dynamics to the radiative transfer problem, resulting in a major advance (Stein & Nordlund 1989; Nordlund, Stein, & Asplund 2009). Descriptions of granule-size, flow magnitude, and line-formation and many other surface details improved considerably. Even 3D LES with MHD in a limited volume have allowed sunspot simulations to become feasible (Rempel, et al. 2009; Kritsuk, et al. 2011).

Despite successes at the surface (depth $< 10^8\text{cm}$) for a quiet, nonrotating Sun, there are problems with velocity at greater depth. Gizon & Birch (2012); Hanasoge, Gizon & Sreenivasan (2016); Greer, et al., (2015) summa-

size evidence suggesting that the amplitude and depth scaling of the convective velocity are in serious question.

Our ILES may give insight, having higher Re and using different methods. In §2, Fig. 2, the bottleneck effect was illustrated for the spectrum of turbulent velocity; while small for our ILES, it is larger for hyperviscosity LES. The strategy for hyperviscosity methods is to add a large, high order dissipation at the grid level to avoid steep gradients. However we find that *turbulent dissipation is due to mild shocks*, so the turbulent cascade would be truncated by hyperviscosity at small scales, as shown in Fig. 2. Shocks captured with pseudo-viscosity will also be smeared, requiring more zones for a given Re .

In our ILES we find strongly nonlocal flow, with threads and filaments forming with increasing *Reynolds* number Re (see Fig. 1 and movies referred to in §2.2.1). We find intermittency to be a fundamental feature, with filamentary structure increasing with Re (Fig. 1). Our ILES agrees fairly well with the dissipation of converged DNS at similar Re (Fig. 2).

Spruit (1997) suggested that a new paradigm for turbulence was needed to deal with the depth problem, and presented one inspired by experimental work of Libchaber and associates with liquid helium, which were interpreted as strongly nonlocal flow, with threads and filaments formed at the boundaries. These experiments (Heslot, Castaing, & Libchaber 1987; Castaing, Gunaratne, Heslot, et al. 1989; Wu & Libchaber 1992) give insight into flows of large *Rayleigh* number (up to $Ra \sim 10^{14}$), but with nonslip boundaries. However, stellar boundaries are “free-slip”, and differ drastically between external (atmospheres) and internal cases. Brandenburg (2016) connects these inconsistencies with *entropy rain* which accompanies the large negative kinetic energy flux at high stratification. It seems likely that simulations of high Re could preserve such features.

Greer, Hindman & Toomre (2016) have introduced a dynamic time delay into their analysis and infer “a downflow rate consistent with anelastic simulations and inconsistent with a 3D cellular structure”. However, from their Fig. 3 & 4, the flow may be consistent with the intermittent plume geometry which we find at high Re . The trajectories of these descending plumes should be arcs, as they tend to conserve specific angular momentum (Arnett & Meakin 2010) and are intermittent. Viscosity (low Re) tends to smear such plumes; high Re seems to allow more coherence (descending tendrils to a shear layer, and interaction between intermittency and rotation?).

Perhaps problems at depth should be no great surprise; any extrapolation from $Re < 100$ (STAGGER)²⁶ to $Re \sim 10^{14}$ (Sun) requires support. We may begin to extrapolate to higher Re using our presently available (but still meager²⁷) resolution study (Cristini, et al. 2017, 2019; Arnett, et al. 2015; Arnett, et al 2019).

7. SUMMARY

In this paper, and Paper I (Arnett, et al 2019), we have analyzed stellar convection theory with our library of implicit large eddy simulations (ILES) of 3D compressible turbulence (using realistic physics for stellar interiors) which have no restrictions for the classical Böhm-Vitense (1958) problem other than zoning.

Our ILES method is supported by new developments both in mathematics (De Lellis & Sze’kelyhidi 2013; Buckmaster & Vicol 2019; Constantin & Titi 1994; Isett 2019) and in physics (Eyink & Drivas 2018a,b; Eyink & Sreenivasan 2006; Sreenivasan 2019; P. Johnson 2021a), related to the Onsager conjecture (Onsager 1949) and “dissipative anomalies”. We solve the Euler equations, appropriate to stars (Fig. 1), which are the high Reynolds number (inviscid) limit of the Navier-Stokes equations. At the zone level, the nonlinear Riemann problem is solved by a high order shock-capturing algorithm (PPM, Colella & Woodward 1984), giving Hölder continuity. In our ILES, dissipation occurs by *nonlinear fluid dynamics*, without requiring a pseudo-viscosity or a Navier-Stokes term for molecular viscosity (§3); we term this feature “Onsager damping”. We find that the effective Reynolds number Re^* depends only on zoning (§2.2); finer zoning allows higher Reynolds numbers (lower effective viscosity). We suggest that our ILES represent a numerical approximation to the inviscid limit, or $Re^* \sim 10^4$.

The ILES results compare well with high resolution DNS (Fig. 2) and seem consistent with experimental trends. Essential features of real turbulence develop automatically: intermittency, coherent structures, and turbulent boundary layers (Warhaft 2002; Sreenivasan 2019). These features are called “anomalous” because they go beyond the “universal” theory of a turbulent cascade (Kolmogorov 1941), but are present in experiment, in DNS, and in our ILES. The dissipation rates

²⁶ $Re^* < 360$ for STAGGER (Magic, Weiss, & Asplund 2016).

²⁷ Our ILES do extend to include the region of “mixing transition” of Dimotakis (2005), i.e., $Re \sim 10^4$. Our dissipation is not parameterized, but is automatically produced by weak shocks from turbulence itself (the “rough” flow of Onsager 1949); see also P. Johnson (2021a).

agree with those of DNS and experiment (see also [Sytine, et al. 2000](#)).

Turbulence is “self-limiting”. The non-linear physics of turbulence determines the rate of conversion of TKE into heat. This dynamically-controlled limit sets the maximum TKE luminosity for a given structure and input luminosity. In turn, this sets a limit for the heat transport by turbulence, which will affect the structure of stars. Excessive luminosity causes vigorous turbulence and shocks, which cause expansion and possibly mass loss by ejection or by winds.

In the weak stratification case, we consider O+O and C+C shells (§4), in which the evolution is accelerated sufficiently for the use of time stepping at the causal (Courant) limit (§2). No assumptions need be made about dissipation, which is calculated self-consistently with turbulence, and confirms our previous analysis. This extends the “universal equilibrium theory” of [Batchelor \(1960\)](#) to a compressible case, in which dissipation is provided by mild shocks from “blowup” of the Euler equations, not NS viscosity.

For strong stratification (§5) we are guided by the red giant simulations of [Viallet, et al. \(2013\)](#). Acceleration by pressure dilatation becomes important. In

the asymptotic limit we find that the turbulent damping length equals the density scale height, on average.

We conclude that the apparent “universality” of the mixing-length ([Renzini 1987](#)) is a consequence of dissipation in deeply stratified convection. Our predicted value of $\alpha_{\text{MLT}} = \ell/H_P \approx 5/3$ fits the data well, if $\pm 20\%$ effects of atmospheres are allowed for, and agrees at that level with estimates involving detailed atmospheres using hyperviscosity approximations ([Trampedach & Stein 2011](#); [Magic, Weiss, & Asplund 2015](#)).

Using hyperviscosity methods to account for shocks in large Re flows, although imperfect (§2), could be adequate to provide a base upon which to build stellar atmospheres ([Trampedach & Stein 2011](#); [Magic, Weiss, & Asplund 2015](#)), but Re should be established before drawing conclusions regarding turbulence, or deeper flows.

We suggest that for astrophysical conditions (very high Re, so $1/\text{Re} \rightarrow 0$), the dominant dissipation occurs by nonlinear fluid flow (shock processes), and that the “molecular” viscosity ν_{NS} commonly used in turbulence theory may not be relevant, its direct effects (e.g., shock thickness) being insignificant at large scales. Both DNS and ILES seem to converge to the same limit in this, the inviscid case (Onsager’s “ideal” turbulence; §2).

APPENDIX

A. EULER AND NAVIER-STOKES EQUATIONS

The Euler equations are: conservation of mass (baryon number): $\partial_t \rho + \nabla \cdot \rho \mathbf{u} = 0$, conservation of momentum: $\partial_t \rho \mathbf{u} + (\rho \mathbf{u} \cdot \nabla) \mathbf{u} = -\nabla P - \rho \mathbf{g}$, and conservation of energy in a co-moving frame: $dE/dt + PdV/dt = dq/dt$. To get the Navier-Stokes equations (which often imply incompressibility) we (i) keep the conservation of mass equation as is, (ii) introduce a new term ($\nu \nabla^2 \mathbf{u}$) in the momentum equation, so

$$\rho \left[\partial_t \mathbf{u} + (\mathbf{u} \cdot \nabla) \mathbf{u} \right] = -\nabla P - \rho \mathbf{g} + \nu \nabla^2 \mathbf{u}, \quad (\text{A1})$$

and (iii) adjust the energy equation to include viscous heating (add $\mathbf{u} \cdot \nu \nabla^2 \mathbf{u}$). See [Landau & Lifshitz \(1959\)](#) and [Pope \(2000\)](#). Setting the Navier-Stokes viscosity ν to zero reverts to the Euler equations, so they are the limit at infinite Re.

The Reynolds number itself is

$$\text{Re} = |(\mathbf{u} \cdot \nabla) \mathbf{u} / \nu \nabla^2 \mathbf{u}| \sim \ell \mathbf{u} / \nu_{\text{NS}},$$

which is the ratio of the inertial term to the dissipation term in the NS equation. There is an important structure factor which is suppressed here in the approximation on the RHS; it is the ratio of the shock (dissipation) width to the viscous damping length (§2.1, §2.2), which is assumed to be unity for the conventional NS equations.

B. THE CODES

The core of our multi-dimensional hydrodynamics code PROMPI is the PROMETHEUS solver written by B. Fryxell, E. Müller and D. Arnett (circa 1988) which is based on the direct Eulerian implementation of PPM ([Colella & Woodward 1984](#)) with generalization to non-ideal gas equation of state. PROMETHEUS also led to the FLASH and VH1 codes. A short history of the PPM algorithm may be found in [Woodward \(2007\)](#); [Porter & Woodward \(2007\)](#). PPM has front steepening, monotonicity (no Gibbs ringing) and low viscosity; the net effect on dissipation appears to be indirect, approaching the inviscid limit through an accurate representation of nonlinear fluid dynamics (§2.1.1).

The implicit MUSIC code is described in detail in [Viallet, et al. \(2011\)](#). Our codes solve the Euler equations, to which we can add nuclear reactions and radiative diffusion through an operator-split formulation.

PROMPI has been adapted to many parallel computing platforms (see below), using domain decomposition, the sharing of a three zone layer of boundary values, and using the MPI message passing library to manage interprocess communication.

PROMPI was designed ([Meakin & Arnett 2007b](#)) to explore nucleosynthesis in deep convection, entrainment, and turbulence. As we saw in §4 it provides a self-calibration, and insight into dissipation as a process, not a parameter. Freed of the computational burden of explicit atmospheres, higher resolution and Reynolds numbers are available.

We may separate the physics of atmospheres into two aspects: (1) line formation and (2) turbulence. We simply accept the first as stated, following [Magic, et al. \(2013\)](#), and examine the second.

[Freytag \(2013\)](#) describes an impressive list of improvements to fluid flow algorithms in CO5BOLD. At least one option (PP) resembles the algorithm in PROMPI ([Meakin & Arnett 2007a](#)), so that CO5BOLD can be free of the problems of hyperviscosity seen in §2. However the computational load of the atmospheric physics implies that useful zoning must be coarse relative to PROMPI, giving a lower effective Re .

CO5BOLD has some notable successes. White dwarf atmospheres have required a variation of MLT, allowing small mixing lengths and shallow stratification. This is a problem for standard MLT but not for 3D simulations (the damping length can be much smaller than a pressure scale height, §4). [Tremblay, et al. \(2015\)](#) find overshoot and departure from hydrostatic equilibrium are needed as well (see also [Cristini, et al. 2017, 2019](#)). Shallow convection is more sensitive to boundary effects ([Arnett, et al. 2015](#)) and steep gradients.

Red giants provide a different challenge: deep stratification. [Ludwig & Kucinskis \(2012\)](#) find a lower region dominated by convection and an upper region by wave activity and shocks. They find no MLT choice of mixing length and turbulent pressure which approximate their LES. This is reminiscent of [Cristini, et al. \(2017, 2019\)](#), who show that for strong driving, the neglected acceleration terms and shocks become important (§3.5).

All the “envelope” entries in Table 5 used LES, and most used the STAGGER hyperviscosity code. [Ludwig, Freytag, & Steffen \(1999\)](#) used the CO5BOLD code. As §4 showed, our ILES automatically satisfy a dynamic constraint which hyperviscosity methods must parameterize.

Regarding the STAGGER code, [Stein & Nordlund \(1989\)](#) note: “Since this is compressible flow, shocks can form. These instabilities are removed and the code is stabilized by applying artificial diffusion to all the fluid equations.” The Re at “stabilization” does not seem to be provided. [Trampedach & Stein \(2011\)](#) construct a “mass-mixing length”, based on stratified flows and LES with the STAGGER hyperviscosity code. Their simulations “have as free parameters only the resolution of the computational grid used and the magnitude of the dissipation used to stabilize the calculations”. These LES use an adjustable viscosity to replace the actual shock dissipation relevant for stellar scales. As we have seen (§4), the turbulent dissipation rate determines flux of turbulent kinetic energy, so that they should not be connected by a freely adjustable parameter.

We thank Dr.-Ing. Andrea Beck, IAGD, Universität Stuttgart, for insightful comments on the manuscript, Axel Brandenburg and Nils Haugen for providing the data from their study, used in our Fig. 2, and Prof. John Lattanzio for vigorous support and guidance for this project, and the Theoretical Astrophysics Program (TAP) at the University of Arizona, and Steward Observatory for support. This work used the Extreme Science and Engineering Discovery Environment (XSEDE), which is supported by National Science Foundation grant number OCI-1053575. Some computations in our work made use of ORNL/Kraken and TACC/Stampede.

AC acknowledges partial support from NASA Grant NNX16AB25G. AC acknowledges the use of resources from the National Energy Research Scientific Computing Center (NERSC), which is supported by the Office of Science of the U.S. Department of Energy under Contract No. DEAC0205CH11231.

The authors acknowledge support from EUFP7ERC2012St Grant 306901. RH acknowledges support from the World Premier International Research Centre Initiative (WPI Initiative), MEXT, Japan. This article is based upon work from the €œChETEC€ COST Action (CA16117), supported by COST (European Cooperation in Science and Technology). CG, RH, and CM thank ISSI, Bern, for their support on organising meetings related to the content of this paper. CG acknowledges support from the Swiss National Science Foundation and from the Equal Opportunity Office of the University of Geneva.

This work used the DiRAC@Durham facility managed by the Institute for Computational Cosmology on behalf of the STFC DiRAC HPC Facility (www.dirac.ac.uk). The equipment was funded by BEIS capital funding via STFC capital grants ST/P002293/1 and ST/R002371/1, Durham University and STFC operations grant ST/R000832/1. This work also used the DiRAC Data Centric system at Durham University, operated by the Institute for Computational Cosmology on behalf of the STFC DiRAC HPC Facility. This equipment was funded by BIS National E-Infrastructure capital grant ST/K00042X/1, STFC capital grants ST/H008519/1 and ST/K00087X/1, STFC DiRAC Operations grant ST/K003267/1 and Durham University. DiRAC is part of the National E-Infrastructure. We acknowledge PRACE for awarding us access to resource MareNostrum 4 based in Spain at Barcelona Supercomputing Center. The support of David Vicente and Janko Strassburg from Barcelona Supercomputing Center, Spain, to the technical work is gratefully acknowledged.

S.W.C. acknowledges federal funding from the Australian Research Council through a Future Fellowship (FT160100046) and Discovery Project (DP190102431). This work was supported by computational resources provided by the Australian Government through NCI via the National Computational Merit Allocation Scheme (project ew6), and resources provided by the Pawsey Supercomputing Centre which is funded by Australian Government and the Government of Western Australia.

REFERENCES

- Aller, L. H., 1963. *Astrophysics: The Atmospheres of the Sun and Stars.*, 2nd. ed., Roland Press Company. New York
- Anderson, J. D., 2005, *Physics Today*, 48, 42
- Arnett, W. D., 1968, *Nature*, 219, 1344
- Arnett, D., 1996, *Supernovae and Nucleosynthesis*, Princeton University Press, Princeton NJ
- Arnett, W. D., Meakin, C., & Young, P. A., 2009, *ApJ*, 690, 1715
- Arnett, W. D. & Meakin, C., 2010, *IAUS* 265, 106
- Arnett, W. D., & Meakin, C., 2011, *ApJ*, 741, 33
- Arnett, W. D., & Meakin, C., 2016, *Reports of Prog. Phys.*, 79, 2901
- Arnett, W. D., Meakin, C. A., Viallet, M., Campbell, S. W., Lattanzio, J. C., Mocák, M., 2015, *ApJ*, 809, 30
- Arnett, W. D., & Moravveji, E., 2017, *ApJ*, 836L, 19
- Arnett, W. D., Meakin, C., Hirschi, R., Georgy, C., Campbell, S., Scott, L., Kaiser, E., Viallet, M., Mocák, M., 2019, (Paper I), *ApJ*, 882, 18
- Asplund, M., Grevesse, N., Sayval, A. J., Scott, P., 2009, *ARA&A*, 47, 481
- Asplund, M, Ludwig, H.-G., Nordlund, Å, Stein, R. F.. 2000, *A&A*, 359, 669
- Baraffe, I., & El Eid, M., 1991, *A&A*, 245, 548
- Batchelor, G. K., 1960, *The Theory of Homogeneous Turbulence*, Cambridge University Press
- Bazàn, G., & Arnett, D. 1998, *ApJ*, 494, 316
- Benzi, R., and Frisch, U., 2010, *Turbulence*, *Scholarpedia*, 5(3):3439
- Biermann, L. 1925, *Zs. Angew. Math.* 5, 136
- Böhm-Vitense, E., 1958, *ZA*, 46, 108

- Böhm-Vitense, E., 1989, *Introduction to Stellar Astrophysics*, Vol. 3, *Stellar Atmospheres*, Cambridge University Press
- Brandenburg, A., 2016, *ApJ*, 832, 6
- Bressan, A.; Marigo, Paola; Girardi, Lèo; Salasnich, Bernardo; Dal Cero, Claudia; Rubele, Stefano; Nanni, Ambra; 2012, *MNRAS*, 427, 127B
- Brown, D. P., Vasil, G. M., & Zweibel, E. G. *ApJ*, 756, 109
- Buckmaster, T., & Vicol, V., 2019, arXiv:1901.09023v2, Convex integration and phenomenologies in turbulence
- Campbell, S. W., Lugaro, M., & Karakas, A., 2010, *A&A* 522, 6
- Castaing, B., Gunaratne, G., Heslot, F., et al. (1989)]castaing Castaing, B., Gunaratne, G., Heslot, F., et al. , 1989, *J. Fluid Mech.* 201, 1
- Chandrasekhar, S., 1939, *An Introduction to the study of Stellar Structure*, University of Chicago Press, Chicago
- Colella, P., & Woodward, P., 1984, *J. Comp. Phys.*, 54, 174
- Constantin, P., & Titi, E. S., 1994, *Commun. Math. Phys.* 165, 207
- Cristini, A., Meakin, C., Hirschi, R., Arnett, W. D., Georgy, C., Viallet, M., Walkington, I., 2017, *MNRAS*, 471, 279
- Cristini, A., Hirschi, R., Meakin, C., Arnett, W. D., Georgy, C., Walkington, I., 2019, *MNRAS*, 484, 464.
- De Lellis, C., & Sze'kelyhidi, L., Jr., 2013, *Dissipative Continuous Euler Flows*, *Invent., Math.*, 193(2):377-407
- Dimotakis, P., 2005, *Ann. Rev. Fluid Mech.*, 37, 329
- Dravins, D. & Nordlund, Å., 1990, *A&A* 228, 203
- Duchon, J., & Robert, R., 2000, *Nonlinearity*, 13, 249
- Ekström, S., Georgy, C., Eggenberger, P., et al., 2012, *A&A*, 537, A146
- Eyink, G., 2018, arXiv:1803.02223
- Eyink, G. & Drivas, T. D., 2018, *Phys. Rev. X* 8.011022
- Eyink, G. & Drivas, T. D., 2018, *Phys. Rev. X* 8.011023
- Eyink, G. L. & Sreenivasan, K. R., 2006, *Rev. Mod. Phys.*, 78, 87
- Falkovich, G., & Sreenivasan, K., 2006, *Phys. Today*, 59, 43.
- Freytag, B., 2013, *Mem. S.A.It. Suppl.* 24, 26
- Frisch, U., 1995, *Turbulence*, Cambridge University Press, Cambridge
- Fryxell, B. A., Müller, E., & Arnett, W. D., 1989,
- Fufimoto, M., Ikeda, Y., & Iben, Icko, Jr., 2000, *ApJ* 529, L25
- Gizon, L., & Birch, A. C., 2012, *PNAS* 109:11896-97
- Grinstein, F., Magolin, L. G., & Rider, W., 2007, *Implicit Large Eddy Simulations*, Cambridge University Press
- Greer, B., Hindmsn, B., Featherstone, N., & Toomre, J., 2015, *ApJ*, 803, L17
- Greer, B., Hindman, B., & Toomre, J., 2016, *ApJ*, 824, 128
- Hanasoge, S. M., Gizon, L., & Sreenivasan, K. R., 2016, *Ann. Rev. Fluid Mech.*, 48, 191
- Haugen, N., & Brandenburg, Axel, 2006, *Phys. Rev. E*, 70, 026405
- Haugen, N., & Brandenburg, Axel, 2006, *Phys. Fluids*, 18, 7, 075106
- Heslot, F., Castaing, B., & Libchaber, A., 1987, *Phys. Rev. A* 36, 5870
- Hoffman, J. & Johnson, Claes, 2008, *BIT Numerical Mathematics*, 48, 285
- Holmes, P., Lumley, J., & Berkooz, G., 1996, *Turbulence, Coherent Structures, Dynamical Systems and Symmetry*, Cambridge University Press
- Isett, P., 2019, *Hölder Continuous Euler Flows in Three Dimensions with Compact Support in Time*, Princeton University Press
- Iyer, K. P., Schumacher, J., Sreenivasan, K. R., Yeung, P. K., *PhRvL*, 121, 26, id.264501
- Johnson, P. L., 2021, *Phys. Rev. Letters* 124, 104501
- Johnson, P. L., 2021, *Physics Today*, 74, 47
- Jones, S., R. Andrassy, S. Sandalski, A. Davis, P. Woodward and F. Herwig, 2017, *MNRAS*, 465, 2991
- Kaneda, Y., Ishihara, T., Yokokawa, K., & Uno, A., 2003, *Physics of Fluids*, 15, L21
- Kippenhahn, R. & Weigert, A. 1990, *Stellar Structure and Evolution*, Springer-Verlag
- Kolmogorov, A. N., 1941, *Dokl. Akad. Nauk SSSR*, 30, 299
- Kritsuk, A., Nordlund, A., Collins, D., Padoan, P., Norman, M., Abel, T., Banerjee, R., Federrath, C., Flock, M., Lee, D., Li, P. S., Müller, W.-C., Teyssier, R., Ustyugov, S., Vogel, C., Xu, H., 2011, *ApJ*, 735, 1
- Landau, L. D. & Lifshitz, E. M., 1959, *Fluid Mechanics*, Pergamon Press, London.
- Leveque, R. J., 2002, *Finite Volume Methods for Hyperbolic Problems*, Cambridge University Press, Cambridge, UK
- Ludwig, H.-G., Freytag, B., & Steffen, M., 1999, *A&A*, 346, 111
- Ludwig, H.-G. & Kucinkas, A., 2012, *A&A*, 547, A118
- Maeder, A., 1999, *Physics, Formation and Evolution of Rotating Stars*, Springer, Berlin
- Magic, Z.; Collet, R.; Asplund, M.; Trampedach, R.; Hayek, W.; Chiavassa, A.; Stein, R. F.; Nordlund, A.; 2013, *A&A*, 557, 26
- Magic, Z.; Collet, R.; Hayek, W.; Asplund, M., 2013b, *A&A*, 560, 8
- Magic, Z., Weiss, A. & Asplund, M., 2015, *A&A*, 573, 89
- Magic, Z., Weiss, A. & Asplund, M., 2016, *A&A*, 586, 88
- Magic, Z.; & Weiss, A.; 2016, *A&A*, 592, A26
- Meakin, C. A., & Arnett, W. D., 2007, *ApJ*, 665, 690
- Meakin, C. A., & Arnett, W. D., 2007, *ApJ*, 667, 448

- Meakin, C. A., & Arnett, W. D., 2010, *Ap&SS*, 328, 22
- Miesch, M. S., Browning, M.K., Brun, A.S., Toomre, J., Brown, B.P., 2009. *Solar-Stellar Dynamos as Revealed by Helio- and Asteroseismology*, eds. M. Dikpati, T. Arentoft, I. González Hernández, C. Lindsey, F. Hill, PASP Conference Series, 416
- Mocák, M., Campbell, S W., Müller, E., & Kifonidis, K., 2010, *A&A*, 510, 114
- Mocák, M., Meakin, C., Viallet, M., & Arnett, D., 2014, arXiv, 1401.5176
- Mocák, M., Meakin, C., Arnett, D., & Campbell, S., 2018, *MNRAS*, 481, 2918
- Mosumgaard, J. R., Ball, W. H., Aquirre, V. S., Weiss, A., Christensen-Dalsgaard, J., 2018, *MNRAS*, 478, 5650
- Muthsam, H. J., Kupka, F., Löw-Daselli, B., et al. , 2010, *New A*, 15, 460
- Nordlund, A., Stein, R., & Asplund, M., 2009, <http://www.livingreviews.org/lrsp-2009-2>
- Onsager, L., 1949, *Statistical Hydrodynamics*. Suppl. al II *Nuovo Cimento*, 6, 279
- Parker, E. N., 1979, *Cosmic Magnetic Fields*, Clarendon Press, Oxford
- Pope, S. B., 2000, *Turbulent Flows*, Cambridge University Press, Cambridge, GB
- Porter, D. H., Anderson, S. E., and P. R. Woodward. 1997, Access, NCSA, <http://www.lcse.umn.edu/research/RedGiant/>
- Porter, D. H. and P. R. Woodward. 2000, *ApJS*, 127, 159
- Porter, D. H., & Woodward, P. R., 2007, in *Implicit Large Eddy Simulations*, ed. F. F. Grinstein, L. G. Margolin, & W. J. Rider, Cambridge University Press, p. 245
- Porter, D. H., & Woodward, P. R., 2007, in *Implicit Large Eddy Simulations*, ed. F. F. Grinstein, L. G. Margolin, & W. J. Rider, Cambridge University Press, p. 439
- Pratt, J., Baraffe, Goffrey T., Constantino, T., Viallet, M., Popov, M. V., Walder, R., Folini, D., 2017, *A&A*, 604, id.A125
- Rempel, M., Schüssler, M., & Knölker, M., 2009 *ApJ* 691, 640
- Renzini, A., 1987, *A&A*, 188, 49
- Richtmeyer, R. D., & Morton, K. W., 1967, *Difference Methods for Initial-value Problems*, 2nd ed., Interscience
- Scott, L. J. A., Hirschi, R., Georgy, C., Arnett, W. D., Meakin, C., Kaiser, E. A., Ekström, S., Yusof., H., 2020, *MNRAS*, in press
- Spruit, H., 1997, *Memorie della Societa Astronomica Italiana* 68, 397
- Sreenivasan, K. R., Antonia, R. A. & Britz, D., 1979, *J. Fluid Mech.* **94**, 745-775
- Sreenivasan, K. R., 2019, *PNAS*, 116 (37) 18175-18183, <https://doi.org/10.1073/pnas.1800436115>
- Stein, R. F., & Nordlund, A., 1989, *ApJ*, 342, 95
- Stein, R. F., Nordlund, A., & Kuhn, J. R., 1989, p. 318, *Solar and Stellar Granulation*, R. J. Rutten and G. Severino (eds.), Kluwer Academic Publishers
- Sytine, I. V., Porter, D. H., Woodward, P. R., Hodson, S. W., Winkler, K.-H., *Journal of Computational Physics* 158 (2000), 225
- Taylor, G. I., 1937, *Journ. Aeronautical Sci.*, 4, 311
- Tennekes, H., & Lumley, J. L., 1972, *A First Course in Turbulence*, MIT Press, Cambridge MA
- Trampedach, R., & Stein, R. F., *ApJ*, 731, 78
- Trampedach, R., Stein, R. F., Christensen-Dalsgaard, J., Nordlund, A., Asplund, M. 2014, *MNRAS*,
- Tremblay, P.-E., Ludwig, H.-G., Freytag, B., Fontaine, G., Steffen, M., and Brassard, P., 2015, *ApJ*, 799, 142
- Vassilicous, J. C., 2015, *Ann. Rev. Fluid Mechanics*, 47:95-114
- Van Dyke, M., 1982, *An Album of Fluid Motion*, Parabolic Press, Stanford, CA
- Viallet, M., Baraffe, I., & Walder, R., 2011, *A&A*, 531, 86
- Viallet, M., Meakin, C., Arnett, D., Mocák, M., 2013, *ApJ*, 769, 1
- Warhaft, Z., 2002, *PNAS* 99, 2481
- Woodward, P. R., 2007, in *Implicit Large Eddy Simulations*, ed. F. F. Grinstein, L. G. Margolin, & W. J. Rider, Cambridge University Press, p. 130
- Woodward, P. R., Porter, D., Herwig, F., Fuchs, T., Nowatzki, A., Pignatari, M., 2007, *AIPC*, 990, 300, *First Stars II Conference*
- Woodward, P. R., Herwig, F., Lin, P.-H., 2015, *ApJ*, 798, 49
- Woodward, P. R., 2006, *PPB*, the Piecewise-Parabolic Boltzmann Scheme for Moment-Conserving Advection in 2 and 3 Dimensions, lcse.umn.edu
- Wu, X.-Z., & Libchaber, A., 1992, *Phys. Rev A*, 45, 842
- Young, P. A., Mamajek, E. E., Arnett, D., Liebert, J., *ApJ*, 556, 230